Macedonian Journal of Chemistry and Chemical Engineering, Vol. **45**, No. 2, pp. xx–xx (2026)

MJCCA9 –

ISSN 1857-5552
e-ISSN 1857-5625

Received: April 15, 2026
Accepted: June 25, 2026

DOI: 10.20450/mjcce.2026.3520
Original scientific paper

GREEN SYNTHESIS OF SILVER NANOPARTICLES USING *SUAEDA VERMICULATA*: CHARACTERIZATION AND EVALUATION OF PHOTOCATALYTIC AND BIOLOGICAL ACTIVITIES

Hadjer Ghalloussi[1], Sameh Boudiba[1], Ibtissam Saouli[1, 2], Louiza Boudiba[1], Karima Hanini[1], Randa Bayoud[1], Ozgur Ceylan[3] and Alfred Ngenge Tamfu[1, 3, 4*]

[1]Laboratory of Applied Chemistry and Renewable Energies (LACRE), Echahid Cheikh Larbi Tebessi University, Constantine Road, 12002, Tebessa, Algeria
[2]Department of Chemistry, Faculty of Sciences, Badji-Mokhtar University, 23000 Annaba Algeria
[3]Food Quality Control and Analysis Program, Ula Ali Kocman Vocational School, Mugla Sitki Kocman University, Mugla 48147, Turkey
[4]Department of Chemical Engineering, School of Chemical Engineering and Mineral Industries, University of Ngaoundere, 454 Ngaoundere, Cameroon

macntamfu@yahoo.co.uk

Silver nanoparticles (AgNPs) were biosynthesized through a green approach using an aqueous extract of the halophyte *Suaeda vermiculata*. In this process, plant phytochemicals acted as natural reducing/capping agents. A surface plasmon resonance band at ~370–480 nm (λmax ≈ 390–400 nm) confirmed AgNP formation. X-ray powder diffraction showed crystalline face-centered cubic silver with reflections at 2θ ≈ 38.12° (111), 44.30° (200), 64.45° (220), and 77.40° (311), with an estimated crystallite size of ~46.6 nm. Scanning electron microscopy revealed predominantly quasi-spherical particles (23.7–57.6 nm; mean ≈ 49.7 nm) with slight aggregation, while atomic force microscopy indicated a nanostructured surface (Ra ≈ 6.25 nm; Rq ≈ 8.85 nm). Energy-dispersive X-ray spectroscopy confirmed the high elemental purity of the nanoparticles, with silver as the major component (≈90.7 wt%). Functionally, AgNPs displayed broad antimicrobial activity (minimal inhibitory concentration [MIC] = 0.156–1.25 mg mL^{-1}) against *Bacillus subtilis*, *Staphylococcus aureus*, *Escherichia coli*, *Salmonella typhi*, and *Candida albicans*, and showed strong dose-dependent antibiofilm inhibition (maximal at the MIC; notably 79.12 % ± 2.45 % against *S. aureus*). Anti-quorum-sensing activity was pronounced: Violacein production in *Chromobacterium violaceum* CV12472 was fully inhibited at the MIC (0.0185 mg mL^{-1}) and remained inhibited at sub-MICs, while *C. violaceum* CV026 exhibited clear quorum-sensing inhibition zones (20.0 ± 1.1 mm at the MIC down to 9.0 ± 1.1 mm at MIC/8). AgNPs also showed moderate antiradical capacity (2,2-diphenyl-1-picrylhydrazyl [DPPH] inhibition 2.73 % at 0.63 mg mL^{-1} to 62.91 % at 40 mg mL^{-1}; half-maximal inhibitory concentration [IC_{50}] ≈ 10–12 mg mL^{-1}). It displayed a modest anti-inflammatory activity in the bovine serum albumin denaturation assay (IC_{50} not reached; estimated 86 ± 9 mg mL^{-1} versus 4.50 ± 0.20 mg mL^{-1} for aspirin), strong cytotoxicity to *Saccharomyces cerevisiae* at ≥ 2.5 mg mL^{-1} (0 % viability; 5.3 % ± 1.5 % at 1.25 mg mL^{-1}), and effective photocatalytic methylene blue removal (~67.40 % after 120 minutes of irradiation). Overall, *S. vermiculata*–derived AgNPs combine controlled nanoscale features with multiple functional activities, namely antibiofilm, quorum-quenching, antioxidant, anti-inflammatory, cytotoxic, and photocatalytic effects.

Keywords: *Suaeda vermiculata*; silver nanoparticles; antibiofilm activity; anti-quorum sensing; cytotoxicity; photocatalytic activity

ЗЕЛЕНА СИНТЕЗА НА СРЕБРЕНИ НАНОЧЕСТИЧКИ СО УПОТРЕБА НА *SUAEDA VERMICULATA*: КАРАКТЕРИЗАЦИЈА И ЕВАЛУАЦИЈА НА ФОТОКАТАЛИТИЧКАТА И БИОЛОШКАТА АКТИВНОСТ

Сребрените наночестички (AgNPs) беа биосинтетизирани со примена на зелен пристап, користејќи воден екстракт од халофитното растение *Suaeda vermiculata*. Во овој процес, фитохемиските соединенија од растението дејствуваа како природни редукциски и стабилизацирачки средства. Формирањето на AgNPs беше потврдено со појава на лента на површинска плазмонска резонанца во опсег од приближно 370–480 nm (λmax ≈ 390–400 nm). Прашкаста дифракција на рендгенските зраци покажа дека среброто има кристална структура од типот кубна површински центрирана решетка, со дифракциски рефлекси при 2θ ≈ 38,12° (111), 44,30° (200), 64,45° (220) и 77,40° (311), при што проценетата големина на кристалите изнесуваше приближно 46,6 nm. Скенирачката електронска микроскопија откри претежно квазисферични честички (23,7–57,6 nm; средна големина ≈ 49,7 nm) со мала тенденција кон агрегација, додека микроскопијата заснована на меѓуатомски сили укажа на наноструктурирана површина (Ra ≈ 6,25 nm; Rq ≈ 8,85 nm). Енергетски дисперзивната рендгенска спектроскопија ја потврди високата елементна чистота на наночестичките, при што среброто беше главна компонента (≈ 90,7%). Во однос на функционалните својства, AgNPs покажаа широк антимикробен спектар на дејство, со минимална инхибиторна концентрација (MIC) од 0,156 до 1,25 mg mL^{-1}, против *Bacillus subtilis*, *Staphylococcus aureus*, *Escherichia coli*, *Salmonella typhi* и *Candida albicans*. Исто така, беше забележана изразена, дозно зависна инхибиција на биофилмот, со максимален ефект при MIC, особено против *S. aureus* (79,12 % ± 2,45 %). Беше забележана изразена инхибиција на сензирањето на кворумот: продукцијата на виолацеин кај *Chromobacterium violaceum* CV12472 беше целосно инхибирана при MIC (0,0185 mg mL^{-1}), а инхибицијата се задржа и при субинхибиторни концентрации (суб-MIC). Кај *C. violaceum* CV026 беа забележани јасно изразени зони на инхибиција на сензирањето на кворумот, со дијаметар од 20,0 ± 1,1 mm при MIC, кој се намали до 9,0 ± 1,1 mm при MIC/8. AgNPs покажаа и умерен антирадикалски капацитет, со инхибиција на 2,2-дифенил-1-пикрилхидразилот (DPPH) од 2,73 % при концентрација од 0,63 mg mL^{-1} до 62,91 % при 40 mg mL^{-1}; половичната максимална инхибиторна концентрација [IC_{50}] изнесуваше приближно 10–12 mg mL^{-1}. Во тестот за денатурација на говедскиот серумски албумин беше утврдена умерена антиинфламаторна активност, при што IC_{50} не беше достигната; проценетата вредност изнесуваше 86 ± 9 mg mL^{-1}, во споредба со 4,50 ± 0,20 mg mL^{-1} за аспиринот. Беше забележана и изразена цитотоксичност кон *Saccharomyces cerevisiae* при концентрации ≥ 2,5 mg mL^{-1} (вијабилност од 0 %; 5,3 % ± 1,5 % при 1,25 mg mL^{-1}), како и ефикасно фотокаталитичко отстранување на метиленското сино (приближно 67,40 % по 120 минути озрачување). Севкупно, AgNPs добиени од *S. vermiculata* ги комбинираат контролирани нанодимензионални карактеристики со повеќе функционални активности, вклучувајќи инхибиција на биофилмот, инхибиција на сензирањето на кворумот, антиоксидациско, антиинфламаторно и цитотоксично дејство, како и фотокаталитичка активност.

Клучни зборови: *Suaeda vermiculata*; сребрени наночестички; антибиофилмна активност; инхибиција на сензирањето на кворумот; цитотоксичност; фотокаталитичка активност

1. INTRODUCTION

Nanoparticles have found wide applications in diagnostics, biomedical implants, pharmaceutical products, tissue engineering, disease prevention, and nanomedicine due to their unique physicochemical properties.[1,2] Among their key biological properties are strong antimicrobial, anti-inflammatory, antioxidant, and anticancer activities.[3,4] Recently, gold, silver, zinc oxide, copper oxide, zirconium oxide, iron oxide, and yttrium oxide nanoparticles synthesized in an environmentally friendly manner have demonstrated antibacterial activity.[5] Besides biological applications, nanomaterials are increasingly recognized for their cost-effective and efficient photocatalytic performance—for example, for wastewater treatment, air disinfection, and hydrogen production.[6,7] Nanomaterials with photocatalytic activity are utilized as sustainable solutions to address the removal of persistent pollutants that extends from the air to the soil.[8] In the presence of a nanophotocatalyst, solar energy can be effectively harnessed to drive chemical transformations, including pollutant degradation, biomass conversion into fuel, and water purification processes.[7,9] These properties arise from the high surface-to-volume ratio and size-dependent electronic and surface characteristics of nanoparticles, which enable functionalities not observed in bulk materials.[10]

Silver nanoparticles (AgNPs) exhibit considerable biological activities due to of their small size, large surface area, and special physicochemical characteristics, which enable them to interact with biological systems efficiently.[8,11] Among metallic nanomaterials, AgNPs are especially prominent due to their broad-spectrum antimicrobial activity and multitarget modes of action (e.g., membrane disruption, protein/enzyme interference, and oxidative stress), which can reduce the likelihood of rapid resistance compared with single-target agents.[12] There is an urgent need for alternative antimicrobials due to antimicrobial resistance, particularly in biofilm-associated infections, where the extracellular polymeric matrix restricts drug diffusion and biofilm cells display heightened tolerance.[13] In parallel, quorum sensing (QS) controls community behaviors such as virulence factor production, secondary metabolite synthesis, and biofilm formation; therefore, quorum-quenching strategies are increasingly explored to attenuate pathogenicity and weaken biofilms without relying solely on killing cells.[14] Due to their extensive antibacterial and photocatalytic capabilities, AgNPs have attracted considerable interest in nanotechnology.[15] However, there are problems with their synthesis, stability, scalability, and environmental sustainability, particularly when employing traditional chemical and physical techniques. Although AgNPs can be produced by conventional physicochemical routes, these methods may require hazardous reducing/stabilizing reagents.[16] Consequently, green synthesis has emerged as a safer and more sustainable alternative, where plant metabolites act as both reducing and capping agents, enabling nanoparticle formation while tuning size, shape, and surface chemistry key factors governing biological activity.[17,18] Green or biological synthesis techniques that include the use of phytochemical capping agents are employed as an affordable and environmentally acceptable alternative to address environmental issues and improve the stability and biocompatibility of AgNPs.[19]

Recent studies have highlighted the critical role of phytochemical-mediated synthesis in controlling the physicochemical and biological properties of AgNPs. Plant-derived metabolites, including phenolic compounds, flavonoids, proteins, and polysaccharides, act simultaneously as reducing and stabilizing agents, producing nanoparticles with enhanced colloidal stability and bioactivity. Furthermore, the surface chemistry imparted by these biomolecules strongly influences antimicrobial, antioxidant, and catalytic performance by modulating nanoparticle–biological interactions and electron-transfer processes. Recent investigations have demonstrated that the biological efficacy of AgNPs obtained with green synthesis is closely associated with the nature of the capping agents and their ability to regulate surface reactivity and reactive oxygen species (ROS) generation. These findings emphasize the importance of understanding the relationship between nanoparticle structure, surface chemistry, and functional properties when developing environmentally friendly nanomaterials for biomedical and environmental applications.

In this context, halophytes represent a particularly promising yet underexplored resource for green nanoparticle synthesis. Due to their adaptation to extreme saline environments, halophytes are rich in stress-induced secondary metabolites with strong reducing and stabilizing capabilities.[20] *Suaeda vermiculata*, a halophytic species, has not been extensively investigated for nanoparticle synthesis, especially in relation to multifunctional biological activities and surface-driven mechanisms. While numerous studies have reported nanomaterial-mediated pollutant removal through adsorption-dominated mechanisms,[20–22] comparatively few have combined a halophyte-derived green synthesis route with a multifunctional evaluation spanning antimicrobial, antibiofilm, anti-QS, antioxidant, anti-inflammatory, cytotoxic, and light-driven photocatalytic activities within a single nanoparticle system. This integrated structure–property–activity framework, applied here to an underexplored halophytic species, constitutes the principal novelty of the present work.

2. EXPERIMENTAL

2.1. *Plant collection and extraction*

Suaeda vermiculata was collected from Boukhadra village in the Tebessa region (Eastern Algeria; 35.762720°N, 8.046068°E) in October 2023. Taxonomic identification was performed at the Department of Natural and Life Sciences, Echahid Cheikh Laarbi Tebessi University (Tebessa, Algeria), using the Botanical Garden and Conservatory of the City of Geneva (CJB)/African Plant Database. A voucher specimen was deposited under herbarium number AMA/5.3.2. The air-dried plant material was powdered; then, 100 g was subjected to ultrasonic extraction with 1 L of distilled water for 60 minutes. The mixture was subjected to coarse filtration, passed through cotton, and finally filtered under pressure using Whatman No. 42 filter paper to obtain a clear aqueous extract.

The extract was stored at 4 °C and used within a short period of time to preserve its bioactivity.[16]

2.2. *Synthesis of AgNPs*

A 1 mM silver nitrate ($AgNO_3$) solution was prepared by dissolving 0.1699 g of $AgNO_3$ in 1 L of distilled water, and the solution was protected from light by wrapping the container with aluminum foil. Prior to the reaction, the pH of the extract was adjusted to 8 by the dropwise addition of 0.1 M sodium hydroxide (NaOH) solution under continuous stirring. For nanoparticle synthesis.[23,24] the plant extract was mixed with the 1 mM $AgNO_3$ solution at a ratio of 1:9 (v/v). The $AgNO_3$ solution was added dropwise to the plant extract using a burette to promote homogeneous nucleation and controlled growth of AgNPs. The reaction mixture was stirred continuously using a magnetic stirrer at 60 °C,[18] and the formation of AgNPs was confirmed by the visible color change from pale yellow to dark brown. After completion of the reaction, the mixture was centrifuged at 10,000 rpm for 10 minutes. The supernatant was carefully discarded, and the pellet was washed with distilled water, followed by re-centrifugation. The washing and centrifugation steps were repeated three times to remove impurities and unreacted residues. Finally, the obtained AgNPs were dried in an oven at 50 °C until a dry powder was obtained.[23] Alkaline conditions enhance the deprotonation of phenolic groups in the plant extract, increasing their reducing capacity and promoting efficient reduction of Ag^+ to Ag^0. This also improves nanoparticle stability and limits aggregation.

2.3. *Characterization of AgNPs*

A range of characterization techniques was used to investigate the structural, optical, and surface properties of AgNPs. In brief, colloidal AgNP suspensions were prepared by dispersing the powdered AgNPs in deionized water or methanol prior to analysis.

2.3.1. *Ultraviolet–visible (UV–Vis) spectroscopy*

The optical properties of the AgNPs were analyzed using a UV–Vis absorption spectrophotometer (Thermo Scientific Evolution 220 UV-Visible spectrophotometer, USA) over a wavelength range of 300–500 nm.

2.3.2. *X-ray diffraction (XRD)*

XRD analysis was conducted using a D2 PHASER diffractometer (Bruker AXS SE, Karlsruhe, Germany) to determine the crystalline structure, phase purity, and crystallite size of the AgNPs.

2.3.3. *Scanning electron microscopy (SEM) and energy-dispersive X-ray spectroscopy (EDX)*

The surface morphology and degree of particle aggregation of the synthesized AgNPs were characterized using a scanning electron microscope equipped with EDX (Thermo Fisher Scientific, USA), enabling high-resolution imaging and elemental analysis of the nanoparticle surfaces.

2.3.4. *Atomic force microscopy (AFM)*

An AFM A100 system (A.P.E Research Trieste, Italy) was employed to obtain detailed three-dimensional (3D) surface topography and roughness data. This high-resolution technique enabled precise mapping of the surface characteristics of the AgNPs, providing valuable information on their structural uniformity and surface organization.

2.3.5. *Fourier-transform infrared (FTIR) spectroscopy*

FTIR spectroscopy was conducted to identify the functional groups present on the surface of the synthesized AgNPs. The analysis was performed using a INVENIO-R spectrometer (model 329, Bruker) equipped with a Specac Quest attenuated total reflectance (ATR) accessory with multiple diamond crystals. Spectra were recorded over a broad range from 6000 to 80 cm^{-1} using the mid-infrared, ATR, wide range configuration. Samples were placed directly onto the diamond crystal of the ATR accessory. Data acquisition involved 30 scans at a spectral resolution of 4 cm^{-1}, with Blackman–Harris 3-Term apodization applied. Power spectrum mode was used for phase correction with a phase resolution of 32.

2.4. *Biological assays*

All experiments included appropriate controls. Negative controls consisted of assay systems without AgNPs, while positive controls were selected according to each assay (e.g., aspirin for anti-inflammatory activity). These controls were

used to establish baseline responses and validate experimental outcomes.

2.4.1. *Antiradical activity*

The antiradical activity of AgNPs was evaluated *in vitro* using the 2,2-diphenyl-1-picrylhydrazyl (DPPH) free radical scavenging assay. A control solution without AgNPs was used as a negative control. Ascorbic acid (vitamin C) was used as the standard antioxidant reference. A 0.1 mM DPPH working solution was freshly prepared by dissolving 0.91 mg of DPPH powder (Sigma-Aldrich Darmstadt, Germany) in 23 mL of absolute ethanol (analytical grade) and protected from light to ensure radical stability. AgNPs were dispersed in a 0.1 M acetate buffer–ethanol mixture (1:1, v/v) to enhance solubility and ensure homogeneous mixing. From an initial stock concentration of 40 mg mL^{-1}, serial two-fold dilutions were prepared to obtain final test concentrations of 40, 20, 10, 5, 2.5, and 1.25 mg mL^{-1}, while maintaining a constant ethanol content across all samples (≤ 1 % v/v). The assay was performed in a flat-bottom 96-well microplate by mixing 100 µL of the DPPH solution with 100 µL of each AgNP dilution. Blanks, vehicle controls, and positive controls were included, and all tests were performed in triplicate. The reaction mixtures were incubated in the dark at room temperature (25 ± 2 °C) for 30 minutes to prevent light-induced degradation of DPPH. After incubation, absorbance was measured at 517 nm using a UV–Vis microplate spectrophotometer. Radical scavenging activity was calculated as percentage inhibition using the formula:[25]

$$\text{Inhibition}(\%) = \left(\frac{Abs_C - Abs_S}{Abs_C}\right) \times 100 \qquad (1)$$

where Abs_C is the absorbance of the control (DPPH solution without AgNPs or antioxidant), and Abs_S is the absorbance measured in the presence of AgNPs or the standard. All measurements were performed in triplicate, and the half-maximal inhibitory concentration (IC_{50}; the concentration required to inhibit 50 % of DPPH radicals) was determined for each sample. Vitamin C was analyzed under identical conditions and served as a positive control, enabling a direct comparison of the antioxidant capacity of the AgNPs under standardized assay conditions.[26]

2.4.2. *Photocatalytic activity by photodegradation of methylene blue (MB)*

Photodegradation of MB was evaluated using a 96-well microplate assay in the presence of AgNPs as the photocatalyst. A 100 mg L^{-1} stock solution of MB was prepared in distilled water and subsequently diluted with phosphate-buffered saline (PBS, pH 7.4) to obtain a 10 mg L^{-1} working solution. The AgNPs were dispersed in distilled water and serially diluted to obtain final test concentrations of 1.25, 2.5, 5, 10, 20, and 40 mg mL^{-1}. For each condition, 200 µL of the MB working solution was transferred into the wells of a flat-bottom 96-well microplate, followed by 10 µL of the corresponding AgNP dilution. The mixtures were gently agitated to ensure uniform nanoparticle distribution. Photodegradation was initiated by exposing the microplate to a controlled light source (e.g., a 365 nm UV lamp or a calibrated visible-light simulator), while maintaining a parallel dark control (MB + AgNPs, covered with aluminum foil) to account for non-photo-induced degradation. Control experiments were performed in the absence of nanoparticles and/or light irradiation to confirm that degradation was photocatalytically driven (control experiments performed in the absence of light showed no dye removal). Absorbance at 665 nm was monitored using a microplate spectrophotometer at intervals of 0, 15, 30, 60, 90, and 120 minutes. The percentage of MB degradation was calculated using the following equation:[27]

$$\text{Degradation}(\%) = \left(\frac{A_0 - A_t}{A_0}\right) \times 100 \qquad (2)$$

where A_0 is the initial absorbance at 0 minutes, and A_t is the absorbance measured at each subsequent time point t. All experiments were conducted in triplicate. The data were analyzed to evaluate the effects of time and concentration on photodegradation efficiency and to compare the photocatalytic performance of the AgNPs under identical experimental conditions.[28]

2.4.3. *Cytotoxicity*

The cytotoxic effects of AgNPs were evaluated against *S. cerevisiae* using a spot dilution growth-sensitivity assay. AgNP suspensions were prepared at concentrations of 0.625, 1.25, 2.5, 5, 10, 20, and 40 mg mL^{-1}. Yeast cells were grown overnight in yeast extract peptone dextrose (YPD) broth and subsequently adjusted to a final density of

2×10^7 cells mL^{-1} in sterile potassium phosphate buffer (100 mM, pH 7). Equal volumes of yeast suspension and each AgNP concentration were mixed in sterile 96-well microplates (Thermo Fisher Scientific) and incubated at 37 °C for 30 minutes. Untreated yeast cells mixed with buffer alone served as the negative control. For semi-quantitative assessment, 3-µL aliquots of each treated mixture were spotted in triplicate onto YPD agar plates supplemented with 2 % glucose and incubated at 37 °C for 48 hours. After incubation, yeast growth was recorded using an Epson flatbed scanner, enabling clear visualization of spot intensity and size. The scanned images were analyzed to determine the cytostatic or cytocidal effects of the AgNPs based on the reduction or absence of visible yeast growth compared with the untreated the untreated control.[25]

2.4.4. *Anti-inflammatory activity*

The anti-inflammatory potential of the synthesized AgNPs was evaluated by measuring their ability to inhibit heat-induced denaturation of bovine serum albumin (BSA), a widely used *in vitro* model for screening anti-inflammatory activity. A 0.3 % BSA solution was prepared in Tris-buffered saline (TBS, pH 7.4) and adjusted to pH 6.4. AgNPs were prepared as a stock suspension at 40 mg mL^{-1} and diluted to final concentrations of 40, 20, 10, and 5 mg mL^{-1}. For each test, 1 mL of BSA solution was mixed with the AgNPs suspension and adjusted to a final volume of 2.5 mL with distilled water. The mixtures were incubated at 37 °C for 15 minutes, heated at 70 °C for 10 minutes to induce protein denaturation, and then cooled at room temperature. Aspirin was used as a positive control, while samples without AgNPs served as negative controls. The degree of protein denaturation was determined by measuring turbidity at 660 nm using a UV–Vis spectrophotometer. The percentage inhibition of protein denaturation was calculated according to the following equation:[29]

$$\text{Inhibition (\%)} = \left(\frac{A_c - A_s}{A_c}\right) \times 100 \qquad (3)$$

where A_c is the absorbance of the control reaction and A_s is the absorbance of the sample containing AgNPs or the standard drug.[30] Moderate inhibition of protein denaturation suggests a limited anti-inflammatory effect, likely associated with antioxidant mechanisms rather than direct inhibition of inflammatory pathways. Relatively low activity compared with aspirin indicates that this effect is secondary and concentration-dependent. All experiments were performed in triplicate, and the results are expressed as the mean ± standard deviation.

2.4.5. *Microbial strains*

The microbial strains used in this study included *Staphylococcus aureus* (ATCC 25923), *Bacillus subtilis*, *Escherichia coli* (ATCC 25922), *Salmonella typhi* (ATCC 25922), and *Candida albicans* (ATCC 10239) for the antimicrobial and antibiofilm assays. *Chromobacterium violaceum* strains CV12472 and CV026 were used for the violacein inhibition and anti-QS experiments.

2.4.6. *Determination of antimicrobial activity of AgNPs*

The antimicrobial activity of the AgNPs was assessed by determining the minimum inhibitory concentration (MIC) using the broth microdilution method in 96-well microtiter plates, as previously described.[31] The MIC was defined as the lowest AgNP concentration that produced no visible microbial growth and is expressed in micrograms per milliliter. Mueller–Hinton broth (MHB) was used as the test medium, and the bacterial inoculum was adjusted to 5×10^5 colony-forming units (CFU) mL^{-1}. Briefly, 96-well microtiter plates were loaded with fresh bacterial suspensions in MHB and treated with AgNPs at final concentrations of 5000, 2500, 1250, 625, 312.5, 156.25, 78.125, 39.0625, and 19.53125 µg mL^{-1}, followed by additional two-fold serial dilutions as required. Growth controls (without AgNPs) were included to confirm normal microbial proliferation. Plates were incubated at 37 °C for 24 hours, after which the MIC was determined by visual examination and spectrophotometric measurement.

2.4.7. *Evaluation of the antibiofilm activity of AgNPs*

The antibiofilm activity of the AgNPs was evaluated at the MIC and sub-MICs using a 96-well microtiter plate assay with crystal violet staining, as previously described.[32,33] Briefly, 180 µL of tryptone soy broth (TSB) supplemented with 0.25 % (w/v) glucose was added to each well, followed by 10 µL of fresh microbial cultures (*S. aureus*, *B. subtilis*, *E. coli*, *S. typhi*, and *C. albicans*) and 20 µL of AgNPs at the MIC and sub-MICs. Plates were incubated at 37 °C for 48 hours, and wells containing inoculated medium without AgNPs

served as the control. After incubation, planktonic cells were carefully removed, leaving the adherent biofilm. The attached biofilms were stained with 0.1 % crystal violet for 10 minutes; subsequently, excess dye was discarded, and wells were rinsed to remove unbound stain. To solubilize the biofilm-bound crystal violet, 200 µL of ethanol or 33 % glacial acetic acid was added and left for 30 minutes. Absorbance was measured at 550 nm using a microplate reader (Multiskan FC, Thermo Scientific). Biofilm inhibition percentage was calculated as:

$$\text{Biofilm Inhibition (\%)} = \left(\frac{OD550_{sample} - OD550_{control}}{OD550_{control}}\right) \times 100 \quad (4)$$

2.4.8. *Determination of violacein inhibition against C. violaceum CV12472 by AgNPs*

Inhibition of violacein by the AgNPs was evaluated using a microplate-based assay, as previously reported.[34] An overnight culture of *C. violaceum* CV12472 was adjusted to an optical density of 0.4 at 600 nm. Then, 170 µL of Luria–Bertani (LB) broth was dispensed into each well, followed by 10 µL of the standardized bacterial suspension and 20 µL of AgNPs at the MIC or sub-MICs. Control wells contained LB broth and bacterial cells without AgNPs. The plates were incubated at 35 °C for 24 hours. After incubation, the wells were visually inspected for reduced violacein pigment production, and the absorbance was measured at 585 nm. The percentage inhibition of violacein production was calculated using the following equation:[35]

$$\text{Violacein Inhibition(\%)} = \left(\frac{OD585_{sample} - OD585_{control}}{OD585_{control}}\right) \times 100 \quad (5)$$

2.4.9. *Determination of quorum-sensing inhibition (QSI) zones against C. violaceum CV026 by AgNPs*

The QSI activity of the AgNPs was assessed as previously described[36] using *C. violaceum* CV026 as the biosensor strain. Soft top agar was prepared by dissolving 1.0 g of sodium chloride (NaCl), 2.0 g of tryptone, and 1.3 g of agar in 200 mL of deionized water and keeping the medium molten at a warm temperature. Then, an overnight culture of *C. violaceum* CV026 (100 µL) was mixed with 5 mL of the warm soft agar, followed by the addition of 20 µL of 100 µg mL^{-1} *N*-acylhomoserine lactone (AHL) as an exogenous QS signal. The mixture was gently homogenized and poured as an overlay onto pre-solidified LB agar plates.[37]

2.5. *Statistical analysis*

All biological and photocatalytic assays were performed with at least three independent replicates (n = 3), unless otherwise stated, and the results are expressed as the mean ± standard error of the mean (SEM). The normality of residuals was visually assessed; given the small sample sizes, parametric tests were used as appropriate for the experimental design. For comparisons involving more than two groups (e.g., AgNP concentration series, microbial strains, or sub-MICs within an assay), one-way analysis of variance (ANOVA) was performed, followed by Tukey's honestly significant difference post hoc test for pairwise comparisons. For two-group comparisons (e.g., AgNPs vs. the positive-control standard in the BSA denaturation assay), Student's *t*-test was applied. All statistical analyses were carried out using Minitab 16 (Minitab Inc., Pennsylvania, USA), with $p < 0.05$ considered to be statistically significant. Exact *p*-values or significance letters/asterisks derived from Tukey's test are reported in the corresponding tables and figures.

3. RESULTS AND DISCUSSION

3.1. *Characterization of AgNPs*

3.1.1. *UV–Vis spectroscopy*

Figure 1 presents the UV–Vis absorption spectrum of the synthesized AgNPs, showing a characteristic surface plasmon resonance (SPR) band in the 300–500 nm region, with a maximum around 390–400 nm. This confirms the formation of AgNPs. The position of the SPR peak indicates the formation of small, predominantly spherical nanoparticles, while the moderate band broadening suggests a certain degree of size distribution (polydispersity), typical of plant-mediated synthesis. The presence of phytochemical compounds in the extract likely contributes to both the reduction of Ag^+ ions and the stabilization of the nanoparticles. Overall, the observed SPR behavior confirms the successful green synthesis of stable AgNPs with nanoscale dimensions.[38,39] The relatively blue-shifted SPR maximum observed near 390–400 nm suggests the formation of small and predominantly spherical nanoparticles, because smaller AgNPs typically exhibit plasmon bands at shorter wavelengths compared with larger or

anisotropic particles.[40] The observed SPR behavior further reflects the nanoscale size and high surface-to-volume ratio of the AgNPs, which are key factors governing their interaction with reactive species and biological systems. Overall, the observed plasmonic response strongly supports the successful green synthesis of stable AgNPs and agrees well with previously reported theoretical and experimental studies on silver nanostructures. The UV–Vis results provide robust spectroscopic evidence for nanoparticle formation and colloidal stability.

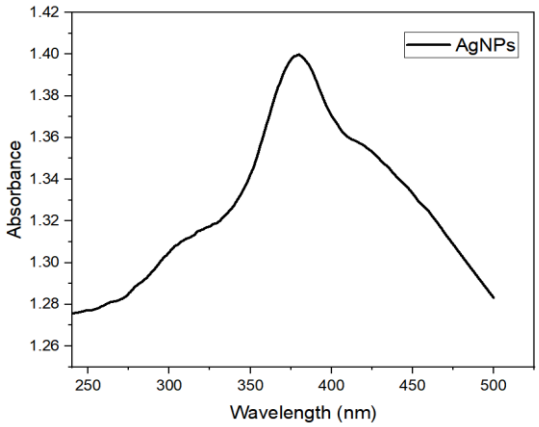


Fig. 1. Ultraviolet–visible absorption spectra of the synthesized silver nanoparticles (AgNPs)

3. 1. 2. *XRD analysis*

Figure 2 displays the XRD pattern of the synthesized AgNPs, recorded over a 2θ range of 0°–90°. The diffractogram exhibits the characteristic reflections of face-centered cubic metallic silver (space group Fm-3m), with the most intense diffraction peak appearing at 2θ ≈ 38.12°, corresponding to the (111) crystallographic plane. There are additional diffraction peaks at 44.30° (200), 64.45° (220), and 77.40° (311), which match well with the standard diffraction data for crystalline silver (JCPDS/ICDD reference code 96-110-0137). The average crystallite size of the AgNPs was estimated using the Debye–Scherrer equation:[41]

$$D = \frac{K\lambda}{\beta \cos\theta} \tag{6}$$

where D is the crystallite size (nm), K is the shape factor (typically 0.9), λ is the wavelength of Cu Kα radiation (0.15406 nm), β is the full width at half maximum of the most intense diffraction peak, and θ is the Bragg angle. The average estimated crystallite size was 46.6 nm. A nanoscale crystallite size is expected to enhance surface reactivity and facilitate electron transfer processes, which are essential for photocatalytic and antimicrobial activities. supporting the nanoscale crystalline nature of the prepared AgNPs.[42] The obtained XRD results clearly demonstrate the successful formation of crystalline, phase-pure, face-centered cubic AgNPs with an average crystallite size in the nanometer range, consistent with previously reported studies on plant-mediated green synthesis of AgNPs. The crystallite size obtained by XRD is consistent with the SPR behavior observed with UV–Vis spectroscopy, further confirming the formation of nanoscale particles.

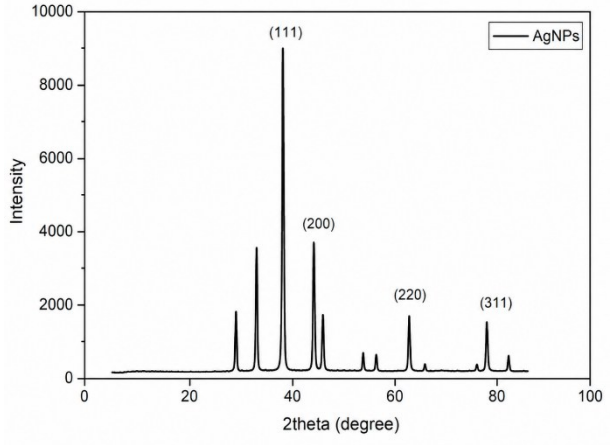


Fig. 2. X-ray diffraction pattern of silver nanoparticles (AgNPs)

3.1.3. *SEM analysis*

SEM images presented in Figure 3 confirm the successful synthesis of AgNPs, as the particles predominantly exhibit a spherical morphology with a relatively uniform shape distribution. The spherical geometry suggests isotropic growth during both the nucleation and growth stages, which is generally associated with the tendency of the system to minimize surface free energy. However, this interpretation should be considered qualitative, as no direct thermodynamic measurements were performed. There is a slight degree of aggregation, which is a common phenomenon in AgNPs due to their high surface energy and strong van der Waals attractive forces between adjacent particles. This aggregation may also be attributed to partial surface coverage by stabilizing biomolecules or their partial removal during washing and drying steps. Similar behavior has been reported previously,[43] where AgNPs exhibited a tendency to aggregate even under controlled synthesis conditions.

A quasi-spherical morphology and small particle size provide a high surface-to-volume ratio, promoting effective interaction with microbial

membranes and enhancing biological activity. Particle size measurements revealed diameters ranging from 23.7 to 57.6 nm, with an average particle size of 49.7 nm. These values are consistent with the crystallite size estimated from XRD analysis, indicating agreement between morphological and structural characterization. From a thermodynamic perspective, the observed morphology and limited aggregation suggest a balance between surface energy minimization and stabilizing interactions provided by phytochemical capping agents. Nevertheless, these considerations remain indicative, and a more rigorous thermodynamic analysis would require additional experimental investigation.

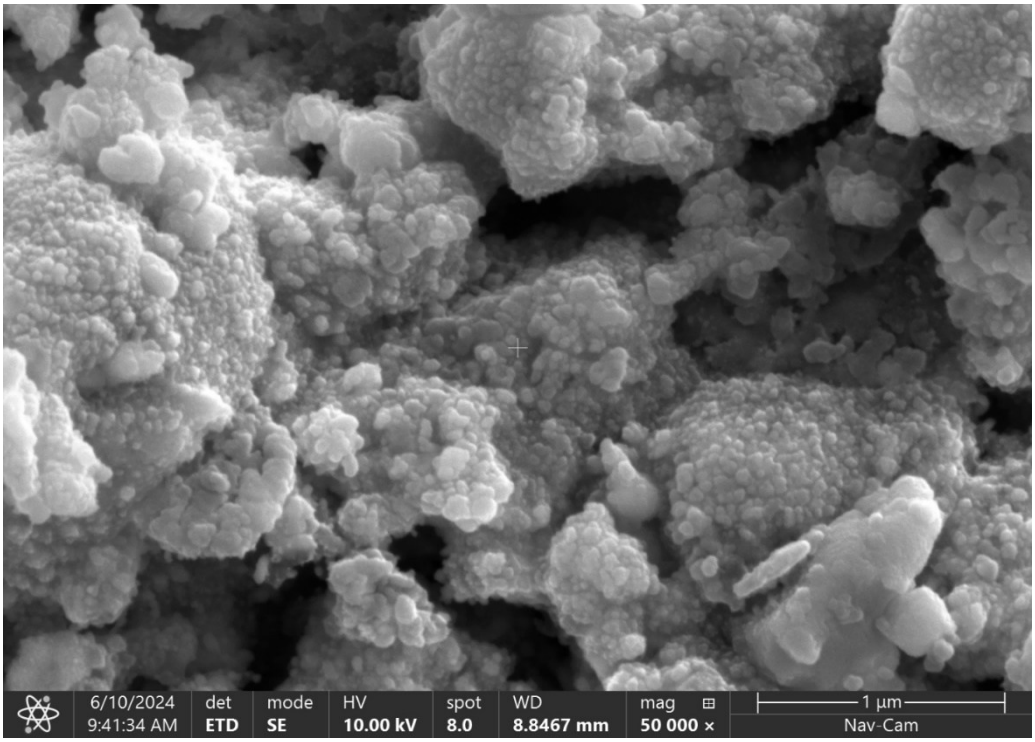


Fig. 3. A scanning electron micrograph of the synthesized silver nanoparticles (AgNPs)

3.1.4. *EDX analysis*

The EDX spectrum (Figure 4a) clearly confirms the successful synthesis and high purity of the AgNPs. There is a strong and intense characteristic peak corresponding to silver, indicating that it is the predominant element in the analyzed sample. The characteristic silver signal around 3 keV further confirms the metallic nature of the AgNPs.

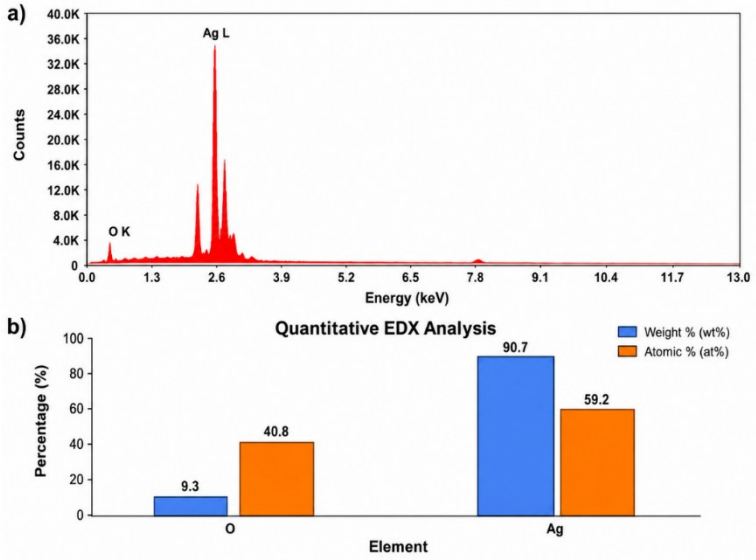


Fig. 4. (a) Energy-dispersive X-ray spectrum of the synthesized silver nanoparticles (AgNPs).
(b) Quantitative EDX analysis of the synthesized AgNPs

As shown in Figure 4b, quantitative EDX analysis revealed that silver is the predominant element, constituting 90.7 wt% (59.2 at%), while oxygen accounts for 9.3 wt% (40.8 at%). The remarkably high silver content demonstrates the efficiency of the green synthesis process in reducing Ag^{+} to Ag^{0} in the AgNPs. The oxygen signal may be attributed to biomolecules adsorbed on the surface of the AgNPs or to oxygen-containing phytochemical compounds acting as stabilizing agents during biosynthesis. Furthermore, the absence of additional impurity peaks in the EDX spectrum confirms the high chemical purity of the synthesized AgNPs. Collectively, these findings provide strong evidence for the successful formation of highly pure AgNPs, achieved through an effective and reliable green reduction pathway with minimal contamination.

There was no significant shift or modification in the structural features after interaction, indicating that the bulk structure remains intact. This suggests that the process is primarily governed by surface-mediated interactions, such as adsorption and interfacial reactions, rather than structural transformation or incorporation into the lattice.

3.1.5. *AFM analysis*

Figure 5 shows the AFM analysis of the synthesized AgNPs. The two-dimensional (2D) image (Figure 5a) shows a relatively homogeneous distribution of nanoscale features without noticeable cracks or major surface defects, indicating uniform surface coverage. Bright regions correspond to elevated nanoparticle domains or clusters, while darker areas represent shallow surface depressions. The 3D topographical reconstruction clearly illustrates the granular surface and vertical height variations across the analyzed area (Figure 5b). Quantitative roughness analysis shows an average roughness (Ra) of 6.25 nm and a root mean square roughness (Rq) of 8.85 nm, confirming a moderately smooth yet nanostructured surface. The relatively low roughness values suggest effective nanoparticle stabilization and homogeneous surface deposition during green synthesis. The maximum peak-to-valley height (Rt ≈ 50 nm) represents the vertical dimension of the surface features and can be correlated with the approximate height of the nanoparticles.[44] Assuming a quasi-spherical morphology, the nanoparticle diameter can be estimated from the AFM height measurements. Because AFM primarily measures vertical topography, a maximum height of approximately 50 nm suggests an estimated particle diameter in the range of 40–50 nm. This estimation is in good agreement with the SEM results. Furthermore, the skewness value (Rsk ≈ −0.11) indicates a nearly symmetrical height distribution with a slight predominance of valleys, while kurtosis (Rku ≈ 4.27) suggests the presence of well-defined peaks characteristic of discrete nanoparticle features. The mean spacing of profile irregularities (Sm ≈ 996 nm) reflects the average lateral separation between nanoparticle aggregates rather than the size of individual particle.[45]

The AFM 2D and 3D analyses confirm the formation of a homogeneous nanostructured silver surface composed of quasi-spherical nanoparticles with an estimated diameter of approximately 40–50 nm, consistent with SEM observations and supporting the successful synthesis of well-defined AgNPs.

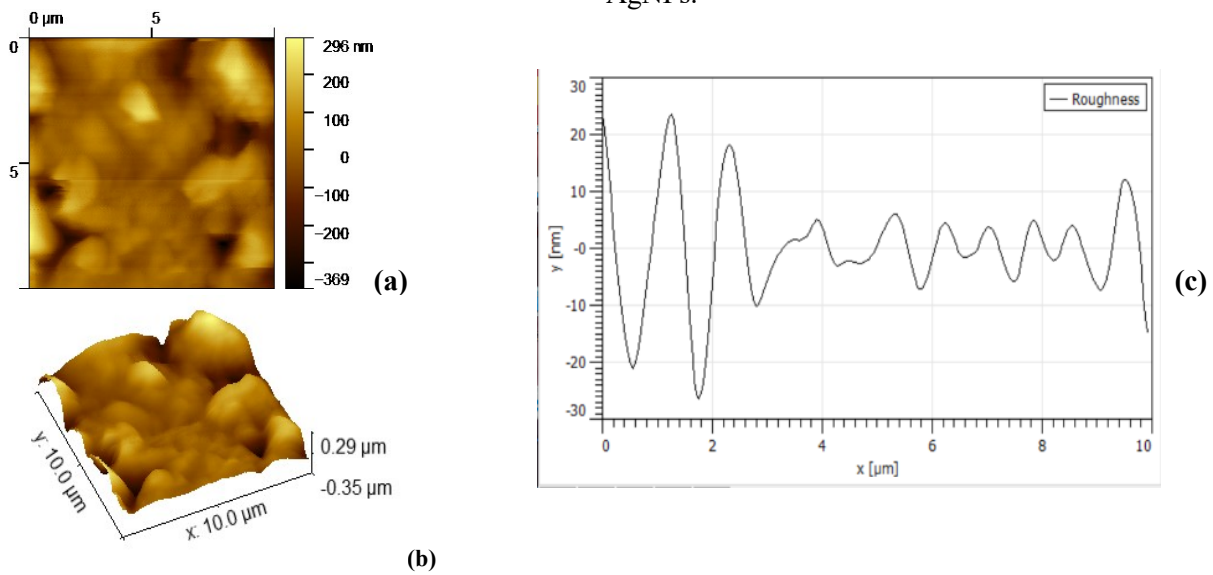


Fig. 5. Atomic force microscopy of the silver nanoparticle (AgNP) film surface: (a) two-dimensional topographic view; (b) three-dimensional topographic view; (c) surface roughness profile

3.1.6. *FTIR spectroscopy*

FTIR spectroscopy was performed to identify the functional groups of biomolecules present on the surface of the synthesized AgNPs that are responsible for reduction and stabilization during green synthesis. The FTIR spectrum in Figure 6 displays several characteristic absorption bands corresponding to plant-derived metabolites. These phytochemical functional groups act as reducing and stabilizing agents and also play a significant role in modulating redox reactions, thereby influencing antioxidant and photocatalytic performance.[46]

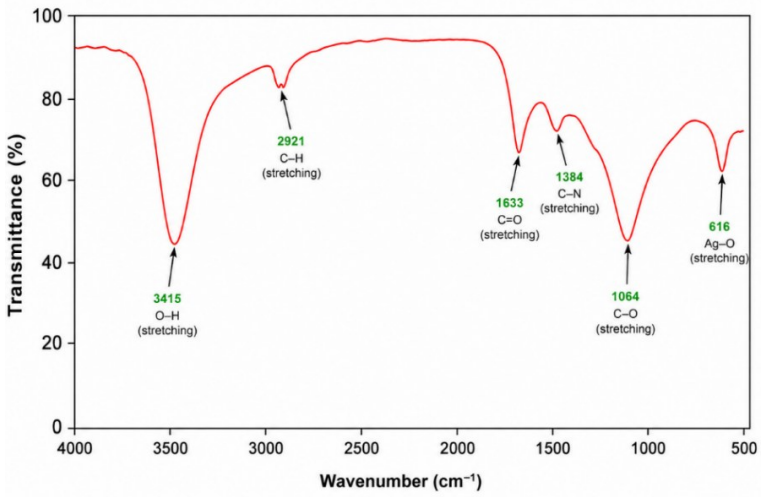


Fig. 6. Fourier-transform infrared spectrum of the synthesized silver nanoparticles

A broad band at ~3400 cm^{-1} is attributed to O–H stretching vibrations of hydroxyl groups in phenolic compounds and alcohols, indicating the presence of polyphenols on the nanoparticle surface. Peaks around 1630–1650 cm^{-1} correspond to C=O stretching vibrations of amide I groups, suggesting that proteins or amino acids from the plant extract contribute to nanoparticle capping. Additional peaks at 1380–1450 cm^{-1} can be assigned to C–N stretching and CH bending vibrations, while the bands at 1050–1100 cm^{-1} indicate C–O stretching from polysaccharides or carbohydrates. The presence of these functional groups confirms that biomolecules from *S. vermiculata* act simultaneously as reducing agents, converting Ag^+ to Ag^0, and as capping/stabilizing agents, preventing nanoparticle aggregation. This behavior is consistent with recent reports on AgNPs obtained via green synthesis, where hydroxyl-, carbonyl-, and amide-containing phytochemicals were identified as key contributors to nanoparticle stabilization and biological activity. The adsorption of these biomolecules on the nanoparticle surface creates a protective organic layer that prevents aggregation while preserving active surface sites. Such surface functionalization has been shown to enhance antioxidant and antimicrobial performance by facilitating electron transfer and promoting interactions with biological targets. Therefore, the FTIR spectroscopy results confirm the participation of plant metabolites in nanoparticle synthesis and also provide insight into the molecular basis of their subsequent biological activities. This observation aligns with the EDX, SEM, and AFM results, which confirm that the AgNPs are crystalline, quasi-spherical, and moderately well dispersed.[47] FTIR spectroscopy provides molecular-level evidence of the green synthesis mechanism, showing that the phytochemicals are involved in both the reduction and stabilization of the synthesized AgNPs, enhancing their colloidal stability and potential biological activity. In particular, hydroxyl and carbonyl groups are known to participate in redox reactions and electron transfer processes, which may enhance antioxidant properties as well as ROS generation during photocatalysis.[35]

Carbonate species may originate from dissolved atmospheric carbon dioxide (CO_2), pH adjustment, or inorganic components present in the plant extract. Under slightly alkaline conditions, such species can form and weakly adsorb onto the nanoparticle surface, potentially contributing to stabilization and influencing surface interactions. However, the FTIR spectrum does not present clear bands characteristic of carbonate species. The weak features observed in the 1400 cm^{-1} region may be attributed either to carbonate species or to overlapping organic functional groups.[46] Therefore, the presence of carbonate species cannot be definitively confirmed but remains plausible considering the synthesis conditions.

3.2. *Biological activities*

3.2.1. *Antiradical activity*

As shown in Figure 7 and summarized in Table 1, the synthesized AgNPs exhibited concentration-dependent DPPH radical scavenging activity. DPPH radical scavenging increased from 2.73 % at 0.63 mg mL^{-1} to 62.91 % at 40 mg mL^{-1}, indicating a progressive enhancement of antioxidant activity as the AgNP concentration increased. There was moderate DPPH radical scavenging activity at intermediate concentrations, namely 27.53 % at 5 mg mL^{-1} and 49.62 % at 10 mg mL^{-1}. The IC_{50} was estimated at 10–12 mg mL^{-1}, suggesting that the synthesized AgNPs possess moderate antioxidant capacity.

Table 1. 2,2-Diphenyl-1-picrylhydrazyl (DPPH) radical scavenging activity of the synthesized silver nanoparticles (AgNPs)

Concentration (mg mL^{-1})	Mean Absorbance	% Inhibition
0.63	1.170	2.73
1.25	1.054	12.35
2.5	1.009	16.13
5	0.872	27.53
10	0.606	49.62
20	0.501	58.32
40	0.446	62.91

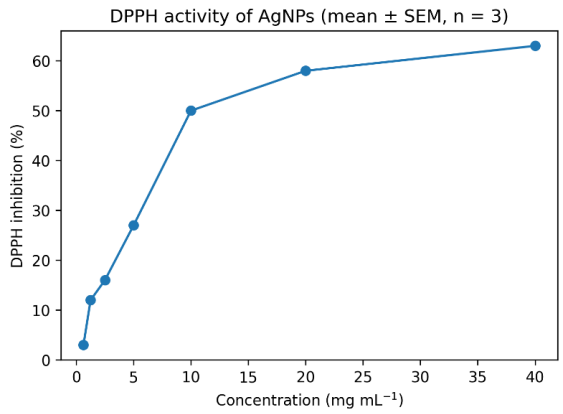


Fig. 7. 2,2-Diphenyl-1-picrylhydrazyl (DPPH) inhibition (%) by the synthesized silver nanoparticles (AgNPs). Negative controls (without nanoparticles) and positive controls (where applicable) are included for comparison. The data are presented as the mean, with the error bars indicting the standard error of the mean (n = 3)

DPPH scavenging activity increased progressively as the AgNP concentration increased, indicating concentration-dependent antioxidant behavior.[48] The observed antioxidant activity can be attributed to the combined effect of nanoparticle surface reactivity and phytochemical capping agents identified by FTIR spectroscopy. These biomolecules can donate electrons or hydrogen atoms to neutralize DPPH radicals, while the nanoscale surface enhances interaction with reactive species.

3.2.2. *Photocatalytic activity*

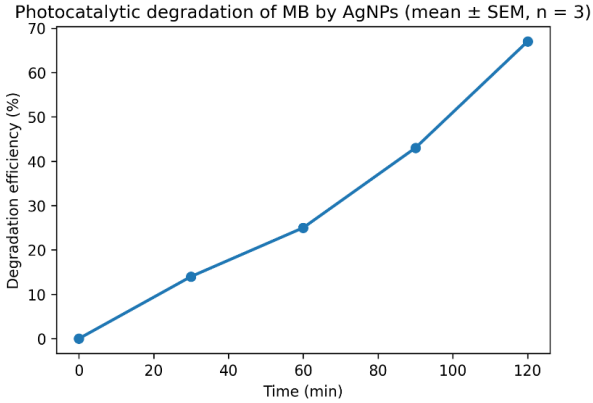


Fig. 8. Time-dependent photocatalytic degradation of methylene blue (MB) under light irradiation in the presence of silver nanoparticles (AgNPs). The data are presented as the mean, with the error bars indicating the standard error of the mean (n = 3)

The photocatalytic degradation of MB under light irradiation in the presence of AgNPs was investigated to evaluate their catalytic performance. The time-dependent degradation profile (Figure 8) shows a gradual increase in removal efficiency, with no significant change observed at the initial stage (t = 0 minutes). This behavior indicates that rapid precipitation or instantaneous adsorption is not the dominant mechanism. Instead, the progressive increase in degradation efficiency suggests a kinetically controlled process, characteristic of surface-mediated photocatalytic reactions.

As summarized in Table 2, there was negligible degradation at t = 0, confirming the stability of the dye before light exposure. Upon irradiation, the degradation efficiency increased gradually to 14.3 % after 30 minutes, suggesting the initiation of photocatalytic reactions at the AgNP surface. Continued irradiation led to a significant increase in degradation efficiency, specifically 24.9 % at 60 minutes and 43.4 % at 90 minutes, demonstrating the progressive breakdown of MB. After 120 minutes, the degradation efficiency was 67.4 %, indicating substantial removal of MB. This enhanced photocatalytic performance can be attributed to the physicochemical properties of AgNPs, including their high surface area and strong interaction with light.[49] Under irradiation, AgNPs facilitate the generation of ROS such as hydroxyl radicals ($^{\bullet}OH$) and superoxide radicals ($O_2^{\bullet-}$). These ROS play a crucial role in the oxidation and

degradation of organic dye molecules into smaller and less harmful compounds.[50,51] Although radical trapping experiments were not performed, this mechanism is consistent with the observed behavior and with widely reported photocatalytic pathways.

Control experiments conducted in the absence of light showed negligible MB removal, confirming that the degradation process is primarily driven by photocatalytic activity rather than adsorption or precipitation alone.

Table 2. Degradation efficiency of methylene blue (MB) by silver nanoparticles (AgNPs) at different irradiation times

Time (min)	Degradation (%)
0	0
30	14.29
60	24.93
90	43.42
120	67.40

To gain deeper insight into the photocatalytic degradation process, the kinetics of MB removal were evaluated using a pseudo-first-order model, which is commonly applied to heterogeneous photocatalytic systems. The kinetic equation is expressed as:[52]

$$\ln\left(\frac{C_0}{C_t}\right) = kt \qquad (7)$$

where C_0 and C_t are the initial and time-dependent MB concentrations, respectively, and k is the apparent rate constant. The results are summarized in Table 3.

Table 3. Pseudo-first-order kinetic parameters for methylene blue (MB) degradation using silver nanoparticles (AgNPs)

Time (min)	Degradation (%)	Ct/C0	ln(C0/Ct)
0	0	1.000	0.000
30	14.29	0.857	0.154
60	24.93	0.751	0.287
90	43.42	0.566	0.570
120	67.40	0.326	1.121

There was a linear relationship between $\ln(C_0/C_t)$ and irradiation time, with an apparent rate constant of $k \approx 0.009$ min^{-1}, and $R^2 \approx 0.91$, indicating a reasonably good fit to the pseudo-first-order model. The agreement with pseudo-first-order kinetics supports degradation that is governed by surface-mediated reactions, characteristic of photocatalytic processes rather than simple precipitation. However, it should be noted that kinetic modeling provides an empirical description and does not, by itself, confirm the exact nature of the interaction.[53] The observed decrease in MB concentration may result from a combination of adsorption, precipitation, and photocatalytic degradation. However, several observations indicate that photocatalysis is the dominant mechanism. First, negligible removal at $t = 0$ suggests that rapid precipitation is not significant. Second, the gradual increase in degradation with irradiation time supports a light-driven process. Therefore, adsorption is likely a preliminary step that facilitates the interaction between dye molecules and reactive surface sites, rather than a competing mechanism. Although precipitation cannot be completely excluded, its contribution is expected to be minor under the studied conditions. Overall, the process is better described as a surface-mediated system involving adsorption–desorption equilibrium followed by photocatalytic degradation.

Competitive adsorption processes also influence the interaction between MB and AgNPs. To contextualize the present findings within recent wastewater-remediation research, three independent studies illustrating how surface-controlled adsorption/kinetic frameworks are applied across different nanomaterial-pollutant systems are mentioned here. First, Godwin et al.[20] examined a calcined zinc oxide (ZnO) nanoadsorbent for the kinetic and thermodynamic study of rhodamine B removal. Second, Kepdieu et al.[21] investigated β-carotene adsorption on silica-smectite composites using a similar kinetic framework. Third, Njimou et al.[22] reported chitin-manganese dioxide (MnO_2)-alginate nanobiocomposite spheres for heavy-metal removal, again analyzed based on equilibrium and kinetic modeling. These studies differ from the present work in nanomaterial composition, synthesis route, and target pollutant, and are cited here solely as methodological precedents demonstrating that surface area, accessible active sites, and adsorption behavior are recurring determinants of removal efficiency across heterogeneous nanomaterial systems not as direct comparators for AgNP structure or bioactivity. In our system, the progressive increase in MB removal under irradiation, together with negligible removal in the absence of light, supports a surface-mediated photocatalytic pathway distinct from the predominantly adsorptive mechanisms reported in these studies. In aqueous systems, dye molecules may compete with other species, such as dissolved ions or solvent molecules, for active sites. Phytochemical capping agents identified by FTIR spectroscopy introduce functional groups (e.g., hydroxyl and carbonyl) that modulate these

interactions by influencing surface charge, adsorption affinity, and accessibility of reactive sites.[54] Furthermore, the accessibility of these functional groups may be affected by steric hindrance, protonation state, and surface orientation. These factors can limit direct interactions and explain the absence or weak detection of certain expected binding features. Overall, the photocatalytic performance reflects a balance between surface chemistry, adsorption behavior, and ROS-mediated degradation.[55]

3.2.3. *Cytotoxicity*

The cytotoxic effects of the synthesized AgNPs on *S. cerevisiae* were evaluated using a spot dilution assay at concentrations ranging from 1.25 to 40 mg mL^{-1}. As summarized in Table 4, yeast cell viability decreased sharply as the AgNP concentration increased.

Table 4. *Saccharomyces cerevisiae* viability (%) after exposure to different concentrations of silver nanoparticles (AgNPs)

Concentration (mg mL^{-1})	Viability (%) AgNPs
S	0.0 ± 0.0
20	0.0 ± 0.0
10	0.0 ± 0.0
5	0.0 ± 0.0
2.5	0.0 ± 0.0
1.25	5.3 ± 1.5
Negative Control	100 ± 0.0

Nearly all tested AgNP concentrations had pronounced cytotoxic effects. At 40, 20, 10, 5, and 2.5 mg mL^{-1}, *S. cerevisiae* viability was 0 %, indicating complete inhibition of cell growth and confirming a strong cytocidal effect. At the lowest tested concentration (1.25 mg mL^{-1}), cell survival was just 5.3 % ± 1.5 %, suggesting that AgNPs retain significant cytotoxic activity even at low doses. In contrast, *S. cerevisiae* treated with the negative control maintained 100 % viability, confirming that the observed effects were directly attributable to AgNP exposure rather than experimental conditions.

The high cytotoxicity of AgNPs can be attributed to well-established mechanisms, including membrane disruption, interaction with intracellular proteins, and the induction of oxidative stress through the generation of ROS.[56,57] These mechanisms collectively lead to cellular damage and loss of viability. Importantly, these results highlight the dose-dependent nature of AgNP activity. While higher concentrations may be particularly effective for antimicrobial and environmental applications, lower concentrations, where limited cell survival is observed, may be more suitable for applications requiring controlled biological activity. Therefore, the cytotoxic behavior of AgNPs should be interpreted in the context of application-specific dosage, emphasizing the need for careful optimization to achieve a balance between efficacy and safety.

3.2.4. *Anti-inflammatory activity*

The anti-inflammatory potential of AgNPs was evaluated based on a heat-induced BSA denaturation assay. As shown in Figure 9, aspirin exhibited a clear dose-dependent inhibition of BSA denaturation, with approximately 50 % inhibition at concentrations of 2.5–5 mg mL^{-1}, with a calculated IC_{50} of 4.50 ± 0.20 mg mL^{-1}, indicating strong anti-inflammatory potency of aspirin. In contrast, AgNPs displayed only moderate inhibition of BSA denaturation, with maximum inhibition remaining below 30 % even at 40 mg mL^{-1}. The IC_{50} was not experimentally reached and was estimated by extrapolation at 86 ± 9 mg mL^{-1}.[58] Nanoparticle concentration appears to play a critical role in determining biological and catalytic performance. At lower concentrations, AgNPs exhibit controlled surface reactivity, enabling antioxidant and moderate anti-inflammatory effects. In contrast, higher concentrations promote excessive ROS generation and nonspecific membrane interactions, resulting in enhanced antimicrobial activity but increased cytotoxicity and reduced anti-inflammatory efficiency.[59] The difference between AgNPs and aspirin was statistically significant (Student's t-test, $p < 0.001$), confirming the superior effectiveness of aspirin in preventing protein denaturation. Nevertheless, the moderate inhibition observed for AgNPs suggests a partial protective effect, possibly related to indirect mechanisms such as antioxidant activity or interactions with protein structure.[58] These results indicate that while AgNPs exhibit some anti-inflammatory potential, their efficacy is considerably lower than that of aspirin under the tested conditions.

3.2.5. *Antimicrobial activity*

As summarized in Table 5, the synthesized AgNPs exhibited broad-spectrum antimicrobial activity against all tested microorganisms, with MICs ranging from 0.156 to 1.25 mg mL^{-1}.

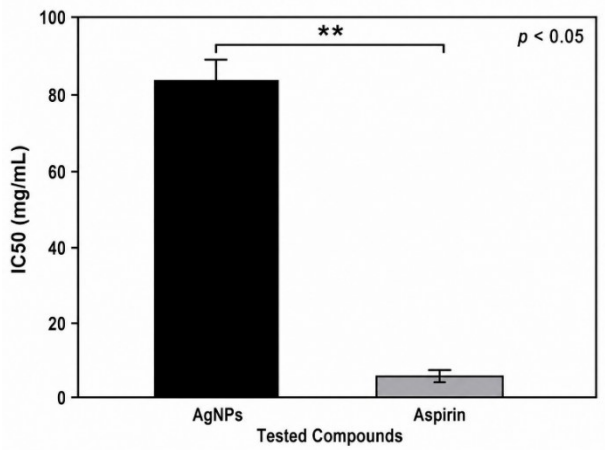


Fig. 9. The half-maximal inhibitory concentration (IC_{50}) of silver nanoparticles (AgNPs) and aspirin in the bovine serum albumin (BSA) denaturation assay. The columns represent the mean, and the error bars indicate the standard error of the mean ($n = 3$). The data were analyzed with one-way analysis of variance (**$p < 0.01$)

The strongest inhibition was observed for *B. subtilis* and *E. coli* (MIC = 0.156 mg mL^{-1} for both), indicating high susceptibility at low AgNP concentrations, while *C. albicans* showed moderate sensitivity (MIC = 0.625 mg mL^{-1}). In contrast, *S. aureus* and *S. typhi* were the least sensitive strains, with a MIC of 1.25 mg mL^{-1}. Overall, the susceptibility trend was *B. subtilis* ≈ *E. coli* > *C. albicans* > *S. aureus* ≈ *S. typhi,* suggesting that AgNPs are effective against gram-positive and gram-negative bacteria as well as yeast, and that the observed variability likely reflects strain-specific differences in cell envelope permeability and stress-response capacity rather than Gram classification alone.

This strain-dependent pattern is consistent with the well-established antimicrobial behavior of metal/metal-oxide nanoparticles, where nanoscale surface area and high reactivity promote strong microbe–nanoparticle interactions.[60,61] In particular, the strong activity observed against *E. coli* aligns with reported mechanisms of AgNPs, which include membrane disruption, interaction with cellular proteins/enzymes, and oxidative stress pathways that collectively inhibit growth and lead to cell death.[62,63] The weaker response of *S. aureus* and *S. typhi* compared with *B. subtilis* and *E. coli* suggests that susceptibility is not governed solely by Gram classification, but also by species-specific differences in cell envelope composition, permeability barriers, and stress-response capacity, which can modulate nanoparticle uptake and tolerance.[60]

Overall, the MIC results in Table 5 provide support for using the synthesized AgNPs as antimicrobial agents, particularly against *B. subtilis* and *E. coli*. They also indicate that higher concentrations may be required to achieve comparable inhibition for more tolerant strains such as *S. aureus* and *S. typhi*. This antimicrobial activity is strongly related to the nanoscale size and surface properties of AgNPs, which facilitate membrane interaction, protein disruption, and oxidative stress induction. The AgNPs exhibited broad-spectrum antimicrobial activity, with variability between strains reflecting differences in cell envelope structure and stress-response mechanisms.

Table 5. Antimicrobial activity (minimal inhibitory concentration [MIC], mg mL^{-1}) of silver nanoparticles

	B. subtilis	***S. aureus***	***E. coli***	***S. typhi***	***C. albicans***
Ag Nps	0.156	1.25	0.156	1.25	0.625

3.2.6. *Antibiofilm activity*

As summarized in Table 6, the synthesized AgNPs demonstrated strong dose-dependent antibiofilm activity against all tested microorganisms, with maximal inhibition at the MIC followed by a progressive decline at MIC/2, MIC/4, and MIC/8 (where available). At the MIC, AgNPs produced the highest biofilm suppression against *S. aureus* (79.12 % ± 2.45 %), indicating a particularly strong antibiofilm effect; there was also substantial inhibition for *B. subtilis* (68.47 % ± 1.12 %) and *C. albicans* (67.59 % ± 0.16 %). In comparison, there was slightly lower but still notable inhibition for *E. coli* (58.58 % ± 0.76 %) and *S. typhi* (57.24 % ± 0.78 %). At lower concentrations, inhibition decreased but remained measurable, notably for *B. subtilis* (42.87 % ± 0.36 % at MIC/2; 27.38 % ± 0.26 % at MIC/4; 12.25 % ± 0.43 % at MIC/8), *S. aureus* (43.28 % ± 1.24 % at MIC/2; 24.58 % ± 0.43 % at MIC/4; 8.78 % ± 0.11 % at MIC/8), and *C. albicans* (34.19 % ± 0.66 % at MIC/2; 18.20 % ± 0.33 % at MIC/4; 6.35 % ± 0.41 % at MIC/8), confirming that the synthesized AgNPs can still interfere with biofilm formation even at sub-MICs. Overall, these results highlight AgNPs as effective antibiofilm agents, with the strongest activity observed against *S. aureus* biofilms and consistent inhibitory trends across decreasing concentrations for most strains.

Table 6. Biofilm inhibition (% inhibition) of the synthesized silver nanoparticles

Bacteria	Sample	MIC	MIC/2	MIC/4	MIC/8
B. subtilis	Ag Nps	68.47±1.12	42.87±0.36	27.38±0.26	12.25±0.43
S. aureus	Ag Nps	79.12±2.45	43.28±1.24	24.58±0.43	8.78±0.11
E. coli	Ag Nps	58.58±0.76	31.64±0.56	10.89±0.49	-
S. typhi	Ag Nps	57.24±0.78	34.53±0.69	15.33±0.81	-
C. albicans	Ag Nps	67.59±0.16	34.19±0.66	18.20±0.33	6.35±0.41

-: No inhibition

The synthesized AgNPs exhibited strong broad-spectrum antimicrobial and antibiofilm activity in this study. In the planktonic growth assay (Table 2), the AgNPs were most potent against *B. subtilis* and *E. coli* (MIC = 0.156 mg mL^{-1}), showed moderate activity against *C. albicans* (0.625 mg mL^{-1}), and were less potent against *S. aureus* and *S. typhi* (MIC = 1.25 mg mL^{-1}), highlighting strain-dependent susceptibility that is often governed by differences in cell-envelope permeability and stress-response capacity rather than Gram classification alone.[14,64] In the antibiofilm assay (Table 3), AgNPs dose-dependently inhibited biofilm formation, with maximal suppression at the MIC, particularly for *S. aureus* (79.12 % ± 2.45 %), followed by *B. subtilis* (68.47 % ± 1.12 %) and *C. albicans* (67.59 % ± 0.16 %), and decreasing inhibition at sub-MICs, with measurable effects for some strains down to MIC/8. This antibiofilm behavior agrees with the reported capacity of nanoparticles to act through multiple pathways (e.g., surface interactions and oxidative stress) and to weaken biofilm integrity and viability.[35,65,66] Specifically for silver, antimicrobial/antibiofilm effects are frequently linked to membrane damage, protein/enzyme inhibition, and oxidative stress mechanisms, which together contribute to growth suppression and disruption of biofilm development.[14,62] The antibiofilm activity may be attributed to the ability of AgNPs to interfere with cell adhesion and disrupt extracellular polymeric substances through surface interactions and oxidative mechanisms. The strong cytotoxic effect is consistent with known mechanisms of AgNP toxicity, including membrane disruption and oxidative stress induced by ROS.[64] The high level of inhibition observed suggests that these processes dominate at the tested concentrations.

Because biofilm formation and virulence factor expression in many bacteria are themselves regulated by QS circuits, we next examined whether the antibiofilm activity of AgNPs reported above is accompanied by a direct effect on QS-controlled phenotypes, using the pigmented biosensor strains *C. violaceum* CV12472 and CV026.

3.2.7. *Violacein inhibition and anti-QS activity*

Chromobacterium violaceum CV12472 produces violacein, a QS-regulated pigment commonly used to monitor QS activity. As summarized in Table 7, the synthesized AgNPs exhibited strong, dose-dependent inhibition of violacein production. AgNPs showed a MIC of 0.0185 mg mL^{-1} and achieved complete suppression (100.00 % ± 0.00 %) of violacein at the MIC. When the concentration was reduced to sub-MICs, violacein inhibition decreased progressively to 72.39 % ± 0.29 % at MIC/2, 39.90 % ± 0.35 % at MIC/4, and 24.85 % ± 0.61% at MIC/8, confirming a clear dose–response relationship.

Table 7. Inhibition of violacein production by *Chromobacterium violaceum* CV12472 exposed to the synthesized silver nanoparticles

Sample	MIC (mg/mL)	MIC	MIC/2	MIC/4	MIC/8
AgNPs	0.0185	100.00±0.00	72.39±0.29	39.9±0.35	24.85±0.61

The marked reduction of violacein production by the synthesized AgNPs suggests a significant anti-QS effect, because violacein biosynthesis in *C. violaceum* is regulated by QS signaling. Importantly, the persistence of substantial inhibition at sub-MICs (e.g., 72 % at MIC/2 and ~25 % at MIC/8) indicates that AgNPs can interfere with QS-regulated pigment production even when the dose is lowered, supporting the interpretation that their effect is not limited to growth suppression alone.[67,68] This behavior is consistent with the established multitarget activity of metal nanoparticles, where surface interactions and redox effects can modulate signaling pathways and QS-controlled phenotypes. Mechanistically, AgNPs may attenuate the production of violacein by

altering membrane integrity and permeability, perturbing cellular redox balance via oxidative stress, and/or interacting with proteins involved in QS regulation and pigment biosynthesis.[69] Overall, the results presented in Table 7 highlight AgNPs as promising agents capable of suppressing QS-related metabolite production in *C. violaceum CV12472* in a strong and dose-dependent manner, which is relevant for reducing QS-driven virulence and biofilm formation.

Table 8. Quorum-sensing inhibition zones in *Chromobacterium violaceum* CV026 exposed to the synthesized silver nanoparticles

Sample	MIC (mg/mL)	MIC	MIC/2	MIC/4	MIC/8
Ag Nps	0.156	20.0±1.1	15.2±0.3	13.5±0.5	9.0±0.1

QSI was assessed using *C. violaceum* CV026, a biosensor strain that produces violacein only when exogenous AHL is available. The appearance of a pigmentless (cream) halo around the wells reflects disruption of QS signal reception/response rather than simple absence of growth. As shown in Table 8, the synthesized AgNPs exhibited clear and concentration-dependent QSI activity, with a maximum inhibition zone of 20.0 ± 1.1 mm at the MIC (0.156 mg mL^{-1}), decreasing to 15.2 ± 0.3 mm at MIC/2, 13.5 ± 0.5 mm at MIC/4, and 9.0 ± 0.1 mm at MIC/8. The persistence of measurable inhibition zones at sub-MICs indicates that AgNPs can interfere with QS even below the concentration required for complete growth inhibition, suggesting a genuine anti-QS effect. This behavior is consistent with reports that nanoparticles can attenuate QS-regulated phenotypes by altering membrane integrity and cellular redox balance and by interfering with signal-mediated regulation, which can ultimately reduce virulence and biofilm establishment.[35,70,71] For AgNPs specifically, multitarget actions such as membrane disruption, binding to thiol-containing proteins/enzymes, and oxidative stress induction may contribute to suppression of QS-controlled pigment expression.[64] Overall, the results support AgNPs as promising QS-disrupting agents with dose-dependent activity against *C. violaceum* CV026, which may be valuable in limiting QS-driven pathogenicity and biofilm-related persistence. The persistence of activity at sub-MIC levels suggests that AgNPs interfere with QS signaling pathways rather than solely inhibiting microbial growth.

The biological and catalytic activities of the synthesized AgNPs can be interpreted within a unified mechanistic framework. Structural characterization (SEM, AFM, XRD) indicates quasi-spherical nanoparticles with high surface area, while FTIR spectroscopy confirms the presence of phytochemical capping agents. These features collectively govern surface-mediated processes, including electron transfer, ROS generation, and interactions with biological membranes. Consequently, antioxidant, antimicrobial, antibiofilm, and photocatalytic activities can be attributed to a combination of nanoscale effects and surface chemistry.

Although phytochemical capping agents are expected to enhance nanoparticle stability, the long-term stability and potential leaching of Ag^+ were not investigated in this study. These factors are important for evaluating both the performance and environmental impact of the nanoparticles. Therefore, further studies focusing on stability assessment and leaching behavior are necessary to ensure safe and sustainable application.

3.3. *Limitations and future directions*

Several limitations of the present study should be acknowledged. First, the proposed ROS-mediated photocatalytic mechanism was inferred from kinetic behavior and dark-control experiments rather than confirmed by radical-scavenger (e.g., isopropanol, benzoquinone, and sodium azide) trapping assays; such experiments are needed to unambiguously identify the dominant reactive species. Second, the long-term colloidal stability of the AgNPs and the extent of Ag^+ leaching under physiologically or environmentally relevant conditions were not assessed, which limits direct extrapolation to real-world biomedical or environmental applications. Third, biological assays were performed on reference microbial strains and a single yeast model; extension to clinical isolates and mammalian cell lines would be required before any biomedical translation is considered. Finally, the gap between the relatively low MICs (0.156–1.25 mg mL^{-1}) and the much higher concentrations that showed cytotoxic and anti-inflammatory activities (≥ 2.5 mg mL^{-1}) highlights the need for dose optimization studies that explicitly map the therapeutic window of *S. vermiculata*–derived AgNPs. Addressing these points together with comparative testing against chemically synthesized AgNPs of matched size

represents a logical next step for this line of research.

4. CONCLUSION

In this study, AgNPs were successfully synthesized via a green, plant-mediated approach using *S. vermiculata* extract and comprehensively characterized in terms of their structural, morphological, optical, and functional properties. UV–Vis spectroscopy confirmed nanoparticle formation through a characteristic SPR band at 390–400 nm, indicating the formation of small and predominantly spherical particles. XRD and SEM/AFM analyses revealed that the AgNPs were crystalline and quasi-spherical, with average sizes ranging from 40 to 50 nm. EDX analysis confirmed their elemental composition, while FTIR spectroscopy revealed the presence of plant-derived biomolecules acting as both reducing and stabilizing agents. Functionally, the synthesized AgNPs exhibited multiple bioactivities, including concentration-dependent antioxidant activity, moderate anti-inflammatory effects, and effective photocatalytic degradation of MB. The photocatalytic process followed pseudo-first-order kinetics, with an apparent rate constant of $k \approx 0.009$ min^{-1} ($R^2 \approx 0.91$), suggesting a surface-mediated degradation mechanism. In addition, the AgNPs demonstrated strong cytotoxic effects against *S. cerevisiae*, but only at concentrations 2–16-fold above the MICs determined against the bacterial and fungal strains tested, indicating a measurable therapeutic window that should be defined more precisely in future dose-ranging studies. AgNPs also showed notable anti-QS activity against *C. violaceum* (CV12472 and CV026), as evidenced by inhibition of violacein production and clear QSI zones, together with dose-dependent antibiofilm activity against all five tested microbial strains.

These results highlight the multifunctional nature of the synthesized AgNPs, combining antimicrobial, antioxidant, and photocatalytic properties. However, the pronounced cytotoxicity and the use of relatively high AgNP concentrations limit direct extrapolation to biomedical applications without further optimization. In addition, aspects such as long-term stability, potential leaching of Ag^+, and performance in complex real matrices were not investigated and should be considered in future studies. It should be emphasized that although the proposed ROS-mediated photocatalytic mechanism is consistent with the observed kinetic and control-experiment data, it was not confirmed by radical scavenger trapping experiments in the present study; this remains an important target for mechanistic validation in future work.

Overall, this work provides a useful basis for understanding the structure–property–activity relationships of AgNPs obtained with green synthesis and highlights the importance of optimizing synthesis conditions and application parameters to balance efficacy and safety for potential environmental and biomedical applications. However, additional studies are required to evaluate the long-term stability of the synthesized AgNPs, possible release of Ag^+, and their performance in complex real water or biological systems.

Acknowledgments: The authors thank Echahid Cheikh Larbi Tebessi University and Mugla Sitki Kocman University for supporting this research.

REFERENCES

(1) Haleem, A.; Javaid, M.; Singh, R. P.; Rab, S.; Suman, R. Applications of Nanotechnology in Medical Field: A Brief Review. *Glob. Health J.* **2023**, *7* (2), 70–77. https://doi.org/10.1016/j.glohj.2023.02.008

(2) Malik, S.; Muhammad, K.; Waheed, Y. Emerging Applications of Nanotechnology in Healthcare and Medicine. *Molecules* **2023**, *28* (18), 6624. https://doi.org/10.3390/molecules28186624

(3) Karunakaran, G.; Sudha, K. G.; Ali, S.; Cho, E.-B. Biosynthesis of Nanoparticles from Various Biological Sources and Its Biomedical Applications. *Molecules* **2023**, *28* (11), 4527. https://doi.org/10.3390/molecules28114527

(4) Bozkurt, S.; Teke, M.; Ceylan, O.; Kayhan, M.; Tamfu, A. N.; Doğaç, Y. İ. Inhibition of Biofilm, Quorum-Sensing, and Swarming Motility in Pathogenic Bacteria by Magnetite, Manganese Ferrite, and Nickel Ferrite Nanoparticles. *Biotechnol. Appl. Biochem.* **2024**, *71* (2), 356–371. https://doi.org/10.1002/bab.2545

(5) Chaudhary, K.; Masram, D. T. Biological Activities of Nanoparticles and Mechanism of Action. In *Model Organisms to Study Biological Activities and Toxicity of Nanoparticles*; Siddhardha, B., Dyavaiah, M., Kasinathan, K., Eds.; Springer: Singapore, 2020; pp 19–34. https://doi.org/10.1007/978-981-15-1702-0_2

(6) Tahir, M. B.; Sohaib, M.; Sagir, M.; Rafique, M. Role of Nanotechnology in Photocatalysis. In *Encyclopedia of Smart Materials*; Olabi, A.-G., Eds.; Elsevier, 2020; 578-589. https://doi.org/10.1016/B978-0-12-815732-9.00006-1

(7) Katre, S.; Baghmare, P.; Giri, A. S. Photocatalytic Nanomaterials and Their Implications towards Biomass Conversion for Renewable Chemical and Fuel Production. *Nanoscale Adv.* **2024**, *6* (21), 5258–5284. https://doi.org/10.1039/D4NA00447G

(8) Hassan, A. S.; Ghadam, P. Photocatalytic Properties of Metal-Based Nanoparticles. In *Handbook of Green and*

Sustainable Nanotechnology; Shanker, U., Hussain, C.M., Rani, M., Eds.; Springer: Cham, 2022. https://doi.org/10.1007/978-3-030-69023-6_22-1

(9) Feliczak-Guzik, A. Nanomaterials as Photocatalysts—Synthesis and Their Potential Applications. *Materials* **2023**, *16* (1), 193. https://doi.org/10.3390/ma16010193

(10) Hussien, N. A.; Khalil, M. A. E. F.; Schagerl, M.; Ali, S. S. Green Synthesis of Zinc Oxide Nanoparticles as a Promising Nanomedicine Approach for Anticancer, Antibacterial, and Anti-Inflammatory Therapies. *Int. J. Nanomed.* **2025**, *20*, 4299–4317. https://doi.org/10.2147/IJN.S507214

(11) Duman, H.; Eker, F.; Akdaşçi, E.; Witkowska, A. M.; Bechelany, M.; Karav, S. Silver Nanoparticles: A Comprehensive Review of Synthesis Methods and Chemical and Physical Properties. *Nanomaterials* **2024**, *14* (18), 1527. https://doi.org/10.3390/nano14181527

(12) Iravani, S. Green Synthesis of Metal Nanoparticles Using Plants. *Green Chem.* **2011**, *13* (10), 2638–2650. https://doi.org/10.1039/C1GC15386B

(13) Tamfu, A. N.; Kucukaydin, S.; Ceylan, O.; Duru, M. E. Evaluation of Enzyme Inhibition and Anti-Quorum Sensing Potentials of *Melaleuca alternifolia* and *Citrus sinensis* Essential Oils. *Nat. Prod. Commun.* **2021**, *16* (9), 1934578X211044565. https://doi.org/10.1177/1934578X211044565

(14) Boudiba, S.; Tamfu, A. N.; Berka, B.; Hanini, K.; Hioun, S.; Allaf, K.; Boudiba, L.; Ceylan, O. Anti-Quorum Sensing and Antioxidant Activity of Essential Oils Extracted from *Juniperus* Species, Growing Spontaneously in Tebessa Region (East of Algeria). *Nat. Prod. Commun.* **2021**, *16* (6), 1934578X211024039. https://doi.org/10.1177/1934578X211024039

(15) Joshi, A. A.; Patil, R. H. Nanoparticles Targeting Biofilms: A New Era in Combating Antimicrobial Resistance. *Med. Microecol.* **2025**, *26*, 100156. https://doi.org/10.1016/j.medmic.2025.100156

(16) Lavecchia, R.; García-Martínez, J. B.; Contreras-Ropero, J. E.; Barajas-Solano, A. F.; Zuorro, A. Antibacterial and Photocatalytic Applications of Silver Nanoparticles Synthesized from *Lacticaseibacillus rhamnosus*. *Int. J. Mol. Sci.* **2024**, *25* (21), 11809. https://doi.org/10.3390/ijms252111809

(17) Khan, F.; Shariq, M.; Asif, M.; Siddiqui, M. A.; Malan, P.; Ahmad, F. Green Nanotechnology: Plant-Mediated Nanoparticle Synthesis and Application. *Nanomaterials* **2022**, *12* (4), 673. https://doi.org/10.3390/nano12040673

(18) Beliatis, M. J.; Gandhi, K. K.; Rozanski, L. J.; Rhodes, R.; McCafferty, L.; Alenezi, M. R.; Alshammari, A. H.; Mills, C. A.; Imalka Jayawardena, K. D. G.; Henley, S. J.; Silva, S. R. P. Hybrid Graphene-Metal Oxide Solution Processed Electron Transport Layers for Large Area High-Performance Organic Photovoltaics. *Adv. Mater.* **2014**, *26* (13), 2078–2083. https://doi.org/10.1002/adma.201304780

(19) Ahmed, S.; Ahmad, M.; Swami, B. L.; Ikram, S. A Review on Plants Extract Mediated Synthesis of Silver Nanoparticles for Antimicrobial Applications: A Green Expertise. *J. Adv. Res.* **2016**, *7* (1), 17–28. https://doi.org/10.1016/j.jare.2015.02.007

(20) Restrepo, C. V.; Villa, C. C. Synthesis of Silver Nanoparticles, Influence of Capping Agents, and Dependence on Size and Shape: A Review. *Environ. Nanotechnol., Monit. Manage.* **2021**, *15*, 100428. https://doi.org/10.1016/j.enmm.2021.100428

(21) Iravani S, Korbekandi H, Mirmohammadi SV, Zolfaghari B. Synthesis of silver nanoparticles: Chemical, physical and biological methods. *Res Pharm Sci.* **2014** Nov-Dec; 9(6):385-406. PMID: 26339255; PMCID: PMC4326978.

(22) Song, J. Y.; Kim, B. S. Rapid Biological Synthesis of Silver Nanoparticles Using Plant Leaf Extracts. *Bioprocess Biosyst. Eng.* **2009**, *32* (1), 79–84. https://doi.org/10.1007/s00449-008-0224-6

(23) Ben Amor, A.; Hemmami, H.; Gherbi, M. T.; Ben Seghir, B.; Zeghoud, S.; Gharbi, A. H.; Chenna, D.; Ben Amor, I.; Alsaeedi, H.; Cornu, D.; Bechelany, M.; Barhoum, A. Synthesis of Spherical Carbon Nanoparticles from Orange Peel and Their Surface Modification with Chitosan: Evaluation of Optical Properties, Biocompatibility, Antioxidant and Anti-Hemolytic Activity. *Biomass Convers. Biorefin.* **2025**, *15* (7), 11345–11358. https://doi.org/10.1007/s13399-024-06291-w

(24) Antunes Filho, S.; dos Santos, M. S.; dos Santos, O. A. L.; Backx, B. P.; Soran, M.-L.; Opriş, O.; Lung, I.; Stegarescu, A.; Bououdina, M. Biosynthesis of Nanoparticles Using Plant Extracts and Essential Oils. *Molecules* **2023**, *28* (7), 3060. https://doi.org/10.3390/molecules28073060

(25) Maurya, S.; Anupam; Tripathi, S.; Chaubey, S.; Soni, A. Recent Advances in the Synthesis and Applications of Zinc Oxide Nanomaterials for Healthcare, Energy and Environmental Systems. *Discov. Chem.* **2026**, *3* (1), 98. https://doi.org/10.1007/s44371-026-00570-3

(26) Kalaycıoğlu, Z.; Özuğur Uysal, B.; Pekcan, Ö.; Erim, F. B. Efficient Photocatalytic Degradation of Methylene Blue Dye from Aqueous Solution with Cerium Oxide Nanoparticles and Graphene Oxide-Doped Polyacrylamide. *ACS Omega* **2023**, *8* (14), 13004–13015. https://doi.org/10.1021/acsomega.3c00198

(27) Said, A. H.; Shaibah, F.; Moustafa, M.; Elamary, R. B. Harnessing Plant Extracts for Zinc Oxide Nanoparticles: A Greener Route to Enhanced Biocompatibility and Therapeutic Potential. *J. Sol-Gel Sci. Technol.* **2026**, *117* (2), 47. https://doi.org/10.1007/s10971-025-07067-y

(28) Nirmala, A.; Permatasari, L.; Muliasari, H.; Deccati, R. Review: Analysis of Optimal Conditions of Bovine Serum Albumin (BSA) Protein Denaturation Inhibition Method in Anti-Inflammatory Activity Testing of Various Plant Leaf Extracts. *J. Agritechnol. Food Process.* **2023**, *3* (2). https://doi.org/10.31764/jafp.v3i2.20953

(29) Tamfu, A. N.; Bozkurt, S.; Ceylan, O. Design and Synthesis of Triazole-Based *p-tert*-Butylcalix[4]arene Conjugates and Evaluation of Their Antimicrobial, Antibiofilm, and Anti-Quorum-Sensing Activities. *Biotechnol. Appl. Biochem.* **2025**, *72* (6), 1546–1559. https://doi.org/10.1002/bab.2761

(30) Benaissa, A.; Wafaa, B.; Tamfu, A. N.; Ammara, B.; Kucukaydin, S.; Latti, N.; Khadir, A.; Bendahou, M.; Anouar, E. H.; Ceylan, O. Inhibition of Clinical Multidrug-Resistant *Pseudomonas aeruginosa* Biofilms by Cinnamaldehyde and Eugenol from Essential Oils: In Vitro and In Silico Analysis. *Chem. Biodiversity* **2025**, *22* (5), e202402693. https://doi.org/10.1002/cbdv.202402693

(31) Merritt, J. H.; Kadouri, D. E.; O'Toole, G. A. Growing and Analyzing Static Biofilms. *Curr. Protoc. Microbiol.* **2011**, *22* (1), 1B.1.1–1B.1.18. https://doi.org/10.1002/9780471729259.mc01b01s22

(32) Koudoro, Y. A.; Tamfu, A. N.; Kucukaydin, S.; Ceylan, O.; Agbangnan Dossa, C. P.; Avlessi, F.; Sohounhloue, C. K. D.; Duru, M. E.; Dinica, R. M. Phenolic Profiles, Antioxidant, Antiquorum Sensing, Antibiofilm and Enzyme Inhibitory Activities of Selected *Acacia* Species Collected from Benin. *LWT* **2022**, *171*, 114162. https://doi.org/10.1016/j.lwt.2022.114162

(33) Ceylan, O.; Tamfu, A. N.; Doğaç, Y. İ.; Teke, M. Antibiofilm and Anti-Quorum Sensing Activities of Polyethylene Imine Coated Magnetite and Nickel Ferrite Nanoparticles. *3 Biotech* **2020**, *10* (12), 513. https://doi.org/10.1007/s13205-020-02509-6

(34) Tamfu, A. N.; Ceylan, O.; Kucukaydin, S.; Ozturk, M.; Duru, M. E.; Dinica, R. M. Antibiofilm and Enzyme Inhibitory Potentials of Two Annonaceous Food Spices, African Pepper (*Xylopia aethiopica*) and African Nutmeg (*Monodora myristica*). *Foods* **2020**, *9* (12), 1768. https://doi.org/10.3390/foods9121768

(35) Manseur, A.; Hanini, K.; Tamfu, A. N.; Boudiba, L.; Arlsan, B. E.; Kucukaydin, M. T.; Ceylan, O.; Benahmed, M.; Boudiba, S. Biogenic Synthesis of ZnO Nanoparticles from *Heliotropium europaeum* and Assessment of Antibiofilm, Anti-Quorum-Sensing, Antioxidant and Anticholinesterase Activities. *Nat. Sci.* **2026**, *6* (2), e70066. https://doi.org/10.1002/ntls.70066

(36) Kelly, K. L.; Coronado, E.; Zhao, L. L.; Schatz, G. C. The Optical Properties of Metal Nanoparticles: The Influence of Size, Shape, and Dielectric Environment. *J. Phys. Chem. B* **2003**, *107* (3), 668–677. https://doi.org/10.1021/jp026731y

(37) Link, S.; El-Sayed, M. A. Size and Temperature Dependence of the Plasmon Absorption of Colloidal Gold Nanoparticles. *J. Phys. Chem. B* **1999**, *103* (21), 4212–4217. https://doi.org/10.1021/jp984796o

(38) Rycenga, M.; Cobley, C. M.; Zeng, J.; Li, W.; Moran, C. H.; Zhang, Q.; Qin, D.; Xia, Y. Controlling the Synthesis and Assembly of Silver Nanostructures for Plasmonic Applications. *Chem. Rev.* **2011**, *111* (6), 3669–3712. https://doi.org/10.1021/cr100275d

(39) Haidari, A. J.; Rahmani, A. H. Zinc Oxide Nanoparticles: A Comprehensive Review on Synthesis and Properties. *Int. J. Curr. Sci. Res. Rev.* **2025**, *8* (7), 3690–3702. https://doi.org/10.47191/ijcsrr/V8-i7-56

(40) Raza, M. A.; Kanwal, Z.; Rauf, A.; Sabri, A. N.; Riaz, S.; Naseem, S. Size- and Shape-Dependent Antibacterial Studies of Silver Nanoparticles Synthesized by Wet Chemical Routes. *Nanomaterials* **2016**, *6* (4), 74. https://doi.org/10.3390/nano6040074

(41) Iravani, S.; Korbekandi, H.; Mirmohammadi, S. V.; Zolfaghari, B. Synthesis of Silver Nanoparticles: Chemical, Physical and Biological Methods. *Res. Pharm. Sci.* **2014**, *9* (6), 385–406.

(42) García, R.; Pérez, R. Dynamic Atomic Force Microscopy Methods. *Surf. Sci. Rep.* **2002**, *47* (6–8), 197–301. https://doi.org/10.1016/S0167-5729(02)00077-8

(43) Wiley, B.; Sun, Y.; Mayers, B.; Xia, Y. Shape-Controlled Synthesis of Metal Nanostructures: The Case of Silver. *Chem. - Eur. J.* **2005**, *11* (2), 454–463. https://doi.org/10.1002/chem.200400927

(44) Pechyen, C.; Tangnorawich, B.; Toommee, S.; Marks, R.; Parcharoen, Y. Green Synthesis of Metal Nanoparticles, Characterization, and Biosensing Applications. *Sens. Int.* **2024**, *5*, 100287. https://doi.org/10.1016/j.sintl.2024.100287

(45) Rajiv, P.; Rajeshwari, S.; Venckatesh, R. Bio-Fabrication of Zinc Oxide Nanoparticles Using Leaf Extract of *Parthenium hysterophorus* L. and Its Size-Dependent Antifungal Activity against Plant Fungal Pathogens. *Spectrochim. Acta, Part A* **2013**, *112*, 384–387. https://doi.org/10.1016/j.saa.2013.04.072

(46) Khatun, H.; Alam, S.; Aziz, M. A.; Karim, M. R.; Rahman, M. H.; Rabbi, M. A.; Habib, M. R. Plant-Assisted Green Preparation of Silver Nanoparticles Using Leaf Extract of *Dalbergia sissoo* and Their Antioxidant, Antibacterial and Catalytic Applications. *Bioprocess Biosyst. Eng.* **2024**, *47* (8), 1347–1362. https://doi.org/10.1007/s00449-024-03029-w

(47) Chong, M. N.; Jin, B.; Chow, C. W. K.; Saint, C. Recent Developments in Photocatalytic Water Treatment Technology: A Review. *Water Res.* **2010**, *44* (10), 2997–3027. https://doi.org/10.1016/j.watres.2010.02.039

(48) Abd-Elkader, O. H.; Deraz, N. M.; Aleya, L. Rapid Bio-Assisted Synthesis and Magnetic Behavior of Zinc Oxide/Carbon Nanoparticles. *Crystals* **2023**, *13* (7), 1081. https://doi.org/10.3390/cryst13071081

(49) Wu, P.-Y.; Jia, Y.; Jiang, Y.-P.; Zhang, Q.-Y.; Zhou, S.-S.; Fang, F.; Peng, D.-Y. Enhanced Arsenate Removal Performance of Nanostructured Goethite with High Content of Surface Hydroxyl Groups. *J. Environ. Chem. Eng.* **2014**, *2* (4), 2312–2320. https://doi.org/10.1016/j.jece.2014.10.010

(50) Muhammad, A.; Kabo, K.; Yushau, A. Visible Light Induced Photocatalytic Removal of Methylene Blue Using Cu-Tunable p-Type ZnO Nanoparticles. *J. Phys. Chem. Funct. Mater.* **2023**, *6* (2), 1-14. https://doi.org/10.54565/jphcfum.1321022

(51) Chakrabarti, S.; Dutta, B. K. Photocatalytic Degradation of Model Textile Dyes in Wastewater Using ZnO as Semiconductor Catalyst. *J. Hazard. Mater.* **2004**, *112* (3), 269–278. https://doi.org/10.1016/j.jhazmat.2004.05.013

(52) Sauer, T.; Cesconeto Neto, G.; José, H. J.; Moreira, R. F. P. M. Kinetics of Photocatalytic Degradation of Reactive Dyes in a TiO_2 Slurry Reactor. *J. Photochem. Photobiol., A* **2002**, *149* (1–3), 147–154. https://doi.org/10.1016/S1010-6030(02)00015-1

(53) Al-Zaban, M. I.; Mahmoud, M. A.; AlHarbi, M. A. Catalytic Degradation of Methylene Blue Using Silver Nanoparticles Synthesized by Honey. *Saudi J. Biol. Sci.* **2021**, *28* (3), 2007–2013. https://doi.org/10.1016/j.sjbs.2021.01.003

(54) Akter, M.; Sikder, M. T.; Rahman, M. M.; Atique Ullah, A. K. M.; Binte Hossain, K. F.; Banik, S; Hosokawa, T.; Saito, T.; Kurasaki, M. A Systematic Review on Silver Nanoparticles-Induced Cytotoxicity: Physicochemical Properties and Perspectives. *J. Adv. Res.* **2018**, *9*, 1–16. https://doi.org/10.1016/j.jare.2017.10.008

(55) Dakal, T. C.; Kumar, A.; Majumdar, R. S.; Yadav, V. Mechanistic Basis of Antimicrobial Actions of Silver Nanoparticles. *Front. Microbiol.* **2016**, *7*, 1831. https://doi.org/10.3389/fmicb.2016.01831

(56) Salve, P.; Vinchurkar, A.; Raut, R.; Chondekar, R.; Lakkakula, J.; Roy, A.; Hossain, M.J.; Alghamdi, S.; Almehmadi, M.; Abdulaziz, O.; Allahyani, M.; Dablool, A. S.; Rahman Sarker, M. M.; Nur Azlina, M. F. An Evaluation of Antimicrobial, Anticancer, Anti-Inflammatory and Antioxidant Activities of Silver Nanoparticles Synthesized from Leaf Extract of *Madhuca longifolia* Utilizing Quantitative and Qualitative Methods. *Molecules* **2022**, *27*, 6404. https://doi.org/10.3390/molecules27196404

(57) Anwar, S.; Almatroodi, S. A.; Almatroudi, A.; Allemailem, K. S.; Joseph, R. J.; Khan, A. A.; Alrumaihi, F.; Alsahli, M. A.; Rahmani, A. H. Biosynthesis of Silver Nanoparticles Using *Tamarix articulata* Leaf Extract: An Effective Approach for Attenuation of Oxidative Stress Mediated Diseases. *Int. J. Food Prop.* **2021**, *24* (1), 677–701. https://doi.org/10.1080/10942912.2021.1914083

(58) Gold, K.; Slay, B.; Knackstedt, M.; Gaharwar, A. K. Antimicrobial Activity of Metal and Metal-Oxide Based Nanoparticles. *Adv. Ther.* **2018**, *1* (3), 1700033. https://doi.org/10.1002/adtp.201700033

(59) Droepenu, E. K.; Amenyogbe, E.; Boatemaa, M. A.; Opoku, E. Study of the Antimicrobial Activity of Zinc Oxide Nanostructures Mediated by Two Morphological Structures of Leaf Extracts of *Eucalyptus robusta* Sm. *Heliyon* **2024**, *10* (4), e25590. https://doi.org/10.1016/j.heliyon.2024.e25590

(60) Li, W.-R.; Xie, X.-B.; Shi, Q.-S.; Zeng, H.-Y.; Ou-Yang, Y.-S.; Chen, Y.-B. Antibacterial Activity and Mechanism of Silver Nanoparticles on *Escherichia coli*. *Appl. Microbiol. Biotechnol.* **2010**, *85* (4), 1115–1122. https://doi.org/10.1007/s00253-009-2159-5

(61) Zhong, L.; Liu, H.; Samal, M.; Yun, K. Synthesis of ZnO Nanoparticles-Decorated Spindle-Shaped Graphene Oxide for Application in Synergistic Antibacterial Activity. *J. Photochem. Photobiol., B* **2018**, *183*, 293–301. https://doi.org/10.1016/j.jphotobiol.2018.04.048

(62) Maksimova, Y. G.; Zorina, A. S. Antibiofilm and Probiofilm Effects of Nanomaterials on Microorganisms (Review). *Appl. Biochem. Microbiol.* **2024**, *60* (1), 1–16. https://doi.org/10.1134/S0003683824010125

(63) Alabresm, A.; Chandler, S. L.; Benicewicz, B. C.; Decho, A. W. Nanotargeting of Resistant Infections with a Special Emphasis on the Biofilm Landscape. *Bioconjugate Chem.* **2021**, *32* (8), 1411–1430. https://doi.org/10.1021/acs.bioconjchem.1c00116

(64) Ikome, H. N.; Tamfu, A. N.; Abdou, J. P.; Fouotsa, H.; Nangmo, P. K.; Lah, F. C. W.; Tchinda, A. T.; Ceylan, O.; Frederich, M.; Nkengfack, A. E. Disruption of Biofilm Formation and Quorum Sensing in Pathogenic Bacteria by Compounds from *Zanthoxylum gilletii* (De Wild) P.G. Waterman. *Appl. Biochem. Biotechnol.* **2023**, *195* (10), 6113–6131. https://doi.org/10.1007/s12010-023-04380-6

(65) Boudiba, S.; Kucukaydin, S.; Tamfu, A. N.; Blaise, K.; Munvera, A. M.; Arab, Y.; Ceylan, O.; Dinica, R. M. HPLC-DAD Phenolic Composition, Antioxidant, Anticholinesterase, Antidiabetic and Anti-Quorum Sensing Properties of Bitter Kola (*Garcinia kola*) and Kolanut (*Cola acuminata*). *Pharmacogn. Res.* **2023**, *15* (2), 373–383. https://doi.org/10.5530/pres.15.2.040

(66) Bayoud, R.; Boudiba, L.; Tamfu, A. N.; Kawther, C.; Arslan, B. E.; Arslan, K.; Hioun, S.; Hanini, K.; Ceylan, O.; Boudiba, S. *Onopordum acaulon* Extracts-Mediated Synthesis of Zinc Oxide Nanoparticles, Evaluation of Cytotoxicity, and Inhibitory Potential of Microbial Biofilm and Quorum Sensing. *J. Chem. Res.* **2026**, *50* (2). https://doi.org/10.1177/17475198261439440

(67) Wang, M.; Lian, Y.; Wang, Y.; Zhu, L. The Role and Mechanism of Quorum Sensing on Environmental Antimicrobial Resistance. *Environ. Pollut.* **2023**, *322*, 121238. https://doi.org/10.1016/j.envpol.2023.121238

(68) Soto-Aceves, M. P.; Diggle, S. P.; Greenberg, E. P. Microbial Primer: LuxR-LuxI Quorum Sensing. *Microbiology* **2023**, *169* (9), 001343. https://doi.org/10.1099/mic.0.001343